Monthly Notices
of the
ROYAL ASTRONOMICAL SOCIETY

MNRAS **473,** 969–983 (2018)
Advance Access publication 2017 September 16

doi:10.1093/mnras/stx2390

The last 6 Gyr of dark matter assembly in massive galaxies from the Kilo Degree Survey

C. Tortora,[1★] N. R. Napolitano,[2] N. Roy,[2,3] M. Radovich,[4] F. Getman,[2] L. V. E. Koopmans,[1] G. A. Verdoes Kleijn[1] and K. H. Kuijken[5]

[1]*Kapteyn Astronomical Institute, University of Groningen, PO Box 800, NL-9700 AV Groningen, the Netherlands*
[2]*INAF – Osservatorio Astronomico di Capodimonte, Salita Moiariello 16, I-80131 Napoli, Italy*
[3]*Dipartimento di Scienze Fisiche, Università di Napoli Federico II, Compl. Univ. Monte S. Angelo, I-80126 Napoli, Italy*
[4]*INAF – Osservatorio Astronomico di Padova, Vicolo Osservatorio 5, I-35122 Padova, Italy*
[5]*Leiden Observatory, Leiden University, PO Box 9513, NL-2300 RA Leiden, the Netherlands*

Accepted 2017 September 11. Received 2017 September 11; in original form 2017 June 26

ABSTRACT

We study the dark matter (DM) assembly in the central regions of massive early-type galaxies up to $z \sim 0.65$. We use a sample of ∼3800 massive ($\log M_\star/\mathrm{M}_\odot > 11.2$) galaxies with photometry and structural parameters from 156 deg^2 of the Kilo Degree Survey (KiDS), and spectroscopic redshifts and velocity dispersions from Sloan Digital Sky Survey (SDSS). We obtain central total-to-stellar mass ratios, $M_{\rm dyn}/M_\star$, and DM fractions, by determining dynamical masses, $M_{\rm dyn}$, from Jeans modelling of SDSS aperture velocity dispersions and stellar masses, $M_\star$, from KiDS galaxy colours. We first show how the central DM fraction correlates with structural parameters, mass and density proxies, and demonstrate that most of the local correlations are still observed up to $z \sim 0.65$; at fixed $M_\star$, local galaxies have larger DM fraction, on average, than their counterparts at larger redshift. We also interpret these trends with a non-universal initial mass function (IMF), finding a strong evolution with redshift, which contrast independent observations and is at odds with the effect of galaxy mergers. For a fixed IMF, the galaxy assembly can be explained, realistically, by mass and size accretion, which can be physically achieved by a series of minor mergers. We reproduce both the $R_{\rm e}$–$M_\star$ and $M_{\rm dyn}/M_\star$–$M_\star$ evolution with stellar and dark mass changing at a different rate. This result suggests that the main progenitor galaxy is merging with less massive systems, characterized by a smaller $M_{\rm dyn}/M_\star$, consistently with results from halo abundance matching.

Key words: galaxies: elliptical and lenticular, cD – galaxies: evolution – galaxies: general – galaxies: structure.

1 INTRODUCTION

Dark matter (DM) dominates the mass density of galaxies and clusters of galaxies. Its budget amounts to ∼85 per cent of the total mass density of the universe (e.g. Abazajian et al. 2003, 2009; Adelman-McCarthy et al. 2008) and its imprint is found at cosmological scales along all cosmic history (e.g. Komatsu et al. 2011). The strongest constraints on the shapes and properties of DM haloes come from numerical simulations of (DM only) structure formation within the consensus cosmology framework, i.e. the Λ cold dark matter (ΛCDM) model (Navarro, Frenk & White 1996, hereafter NFW; Bullock et al. 2001; Macciò, Dutton & van den Bosch 2008). However, more realistic models, which try to account for the effect of baryons on the DM distribution (e.g. Blumenthal et al. 1984; Gnedin et al. 2004; Wu et al. 2014), seem more compatible with observations (e.g. Gnedin et al. 2007; Napolitano, Romanowsky & Tortora 2010) and make more realistic predictions on the expected DM fractions in the central galaxy regions (Ruszkowski & Springel 2009; Hilz, Naab & Ostriker 2013; Wu et al. 2014).

Early-type galaxies (ETGs; ellipticals and lenticulars) contain most of the cosmic stellar mass of the universe, and represent the final stage of galaxy evolution. They hold the fossil record of the stellar and DM assembly through time, and, being the most luminous and massive galaxies, can be studied in details out to large redshifts. In particular, since ETGs are thought to be the product of the transformation of late-type galaxies (LTGs), e.g. through the effect of merging and other feedback mechanisms, they are crucial to understand the processes that shape galaxies across time.

In this context it is important to trace the assembly of both the luminous and the dark components of these systems. For example,

★ E-mail: ctortora@na.astro.it

the total stellar-to-dark mass ratio of ETGs depends strongly on the galaxy mass, and seems to be connected to the overall star formation efficiency (Benson et al. 2000; Marinoni & Hudson 2002; Napolitano et al. 2005; Mandelbaum et al. 2006; van den Bosch et al. 2007; Conroy & Wechsler 2009; Moster et al. 2010; Alabi et al. 2016).

However DM rules also the central galaxy regions (Gerhard et al. 2001; Padmanabhan et al. 2004; Cappellari et al. 2006; Thomas et al. 2007, 2009, 2011; Cardone et al. 2009, 2011; Hyde & Bernardi 2009b; Tortora et al. 2009, 2012, 2014c; Auger et al. 2010; Cardone & Tortora 2010; Shu et al. 2015; Nigoche-Netro et al. 2016), in a way substantially consistent with the concordance ΛCDM scenario (Tortora et al. 2009, 2012; Napolitano et al. 2010). Different works have shown that the central DM fraction (typically within one effective radius, R_e hereafter) is higher in larger and more massive galaxies (e.g. Hyde & Bernardi 2009b; Ruszkowski & Springel 2009; Tortora et al. 2009, 2012; Auger et al. 2010; Napolitano et al. 2010; Thomas et al. 2011), even though there is no universal consensus about such a trend as also pieces of evidence of an anticorrelation with mass have been presented (e.g. Grillo et al. 2009; Grillo 2010; Grillo & Gobat 2010).

The claimed correlation with mass seems almost insensitive to the adopted galaxy mass profile or initial mass function (IMF; e.g. Cardone et al. 2009, 2011; Cardone & Tortora 2010), but it can become uncertain in case a non-ΛCDM scenario, with mass following the (non-homologous) light distribution, is adopted (e.g. Trujillo, Burkert & Bell 2004; Tortora et al. 2009, 2012). The scenario is even more complicated if one takes into account the effect of a non-universal IMF (Treu et al. 2010; van Dokkum & Conroy 2010; Thomas et al. 2011; Cappellari et al. 2012, 2013; Conroy & van Dokkum 2012; Spiniello et al. 2012, 2015; Wegner et al. 2012; Barnabè et al. 2013; Dutton et al. 2013; Ferreras et al. 2013; Goudfrooij & Kruijssen 2013, 2014; La Barbera et al. 2013; Tortora, Romanowsky & Napolitano 2013; Weidner et al. 2013; McDermid et al. 2014; Tortora et al. 2014a,b; Martín-Navarro et al. 2015; Shu et al. 2015; Lyubenova et al. 2016; Tortora, La Barbera & Napolitano 2016; Corsini et al. 2017; Li et al. 2017; Sonnenfeld, Nipoti & Treu 2017; Tortora, Koopmans & Napolitano 2017). Indeed, the IMF remains the largest source of uncertainty to quantify the stellar and DM mass budget in the central galactic regions. In absence of direct constraints (e.g. using gravity sensitive spectral lines; see Spiniello et al. 2012; La Barbera et al. 2013), the adoption of different 'universal' IMF recipes causes the stellar mass to vary by a factor of 2 or more (i.e. assuming a Chabrier 2001 or a Salpeter 1955 IMF or even super-Salpeter IMF; e.g. Tortora et al. 2009) hence strongly affecting the conclusions on the central DM fraction in these extreme cases. In the case of 'non-universality', the systematic variation of the IMF with mass (or velocity dispersion), from a bottom-lighter (i.e. 'lower mass') IMF for low-mass systems to a bottom-heavier (i.e. 'higher mass') IMF in massive galaxies could dilute (and even cancel) the 'apparent' DM fraction trend with mass (e.g. Thomas et al. 2011; Tortora et al. 2013; Spiniello's thesis, chap. 2). However, once again, the scenario is far to be fully constrained as for the most massive galaxies some contrasting results point to unexpected low stellar mass-to-light ratios (M/Ls) and bottom-light IMFs have been found (Smith, Lucey & Conroy 2015).

One way to interpret all these pieces of evidence in the context of the galaxy evolution is to check the persistence of these correlations at higher redshift and find the epochs where these effects start to emerge. This implies a test on the assembly of both the dark and the stellar matter in galaxies, at epochs where (a) both are in an early stage of their evolution and (b) the freedom on some parameters (e.g. age, metallicity of stars, concentration of the DM haloes, etc.) is minimal.

In order to cover the full parameter space, including the lookback time, we need large galaxy samples. So far, most of the DM studies were limited to low-redshift samples, and only recently systematic analysis of high-redshift samples have been started. In some cases the data sets are restricted to small samples and small redshift windows to evaluate the dependence of the galaxy DM content on redshift, as in the case of gravitational lenses (Auger et al. 2009, 2010; Tortora et al. 2010b; Sonnenfeld et al. 2013). The first studies have given contrasting results (Faure et al. 2011; Ruff et al. 2011). The reason of the tensions among these latter studies probably resides in the paucity of the galaxy samples and differences in the model choices.

The first systematic studies of the evolution of the central DM fraction with redshift have been recently performed by Beifiori et al. (2014) and Tortora et al. (2014c), which provided pieces of evidence that high-z ETGs are less DM dominated than their local counterparts.

However, this line of investigations has just started and further independent analyses are needed, not only to constrain the overall evolution of central DM, but also to assess the correlations with structural parameters, mass and stellar density, and evaluate how these change as a function of redshift, within or not the non-universal IMF scenario. To make even a step forward into the previous analysis, we have applied the Jeans method discussed in Tortora et al. (2014c) to a state-of-the-art sample of galaxies covering a broad redshift range for which high-quality imaging and internal kinematics were available, both necessary to characterize the stellar and total mass for these systems. We have gathered a sample of massive galaxies with high-quality imaging, measured structural parameters and stellar masses from the Kilo Degree Survey (KiDS). KiDS is one of the public surveys carried out with the VLT Survey Telescope (VST), which is characterized by the excellent image quality, thanks to the very good seeing (0.65 arcsec, on average, in the r-band) and a high depth in the r band (∼25 mag limiting magnitude). The KiDS fields in the Northern Galactic Cap partially overlap with Sloan Digital Sky Survey (SDSS) Data Release 7 (DR7) data sample and with SDSS/Baryon Oscillation Spectroscopic Survey (BOSS), both of which provided the spectroscopic redshifts and central velocity dispersions for our galaxy sample. Jeans modelling was used to determine dynamical masses and total-to-stellar mass ratios, to be correlated with galaxy parameters and redshift. Our results are also compared with those from (a) low-redshift ($0.05 < z < 0.095$) ETGs from the Spheroid's Panchromatic Investigation in Different Environmental Regimes (SPIDER) project (La Barbera et al. 2010; Tortora et al. 2012), (b) a spectroscopically selected sample of ETGs covering the range of redshifts $z \sim 0.4$–0.8 from the ESO Distant Clusters Survey (EDisCS; Saglia et al. 2010; Tortora et al. 2014c) and (c) other results from literature observations and simulations.

This paper is organized as follows. Data samples and the analysis performed are presented in Section 2. The correlation with structural parameters, mass probe and stellar density are discussed in Section 3. Section 4 is devoted to the systematic analysis of central DM and IMF evolution with redshift, systematics and the interpretation within the merging scenario. A summary of the results, conclusions and future prospects is discussed in Section 5. We adopt a cosmological model with (Ω_m, Ω_Λ, h) = (0.3, 0.7, 0.75), where $h = H_0/100\,\mathrm{km\,s^{-1}\,Mpc^{-1}}$ (Komatsu et al. 2011).

2 ANALYSIS

2.1 KiDS and SDSS data samples

The galaxy sample presented in this work is selected from the data included in the first, second and third data releases of KiDS presented in de Jong et al. (2015, 2017). The total data set includes 156 KiDS pointings with the measured structural parameters presented in Roy et al. (in preparation). We have identified about 22 million sources, including ∼7 million that have been classified as high-quality extended sources. We select those systems with the highest signal-to-noise ratio (S/N) in the r band images, $\mathrm{S/N}_r \equiv 1/\mathrm{MAGERR\_AUTO\_R} > 50$, with reliable structural parameters measured. This data set includes aperture and total photometry, photometric redshifts and structural parameters.

To record spectral information, such as spectroscopic redshifts and velocity dispersions, this data sample is cross-matched with two different SDSS samples, collecting a sample of galaxies with redshifts in the range $0 < z < 0.7$.

(i) *MPA-JHU-DR7*. For the lowest redshifts ($z < 0.2$) we base our analysis on the spectroscopic data from the SDSS DR7 (Abazajian et al. 2009). In particular, we select these systems, getting redshifts and velocity dispersions from the MPA-JHU-DR7 catalogue,[1] which consists of ∼928 000 galaxies of any type with redshifts $z \lesssim 0.7$. The cut in mass that we will perform later will remove almost all the late-type contaminants. Spectra are measured within fibres of diameter 3 arcsec.

(ii) *BOSS-DR10*. Data at redshift $z \geq 0.2$ are taken from the SDSS-III/BOSS Data Release 10[2] (DR10;Ahn et al. 2014). Selection criteria are designed to identify a sample of luminous and massive galaxies with an approximately uniform distribution of stellar masses following the Luminous Red Galaxy (LRG; Eisenstein et al. 2011) models of Maraston et al. (2009). The galaxy sample is composed of two populations: the higher redshift constant mass sample (CMASS; $0.4 < z < 0.7$) and the low-redshift sample (LOWZ; $0.2 < z < 0.4$). The total sample, which consists of 934 000 spectra and velocity dispersions across the full SDSS area, starts to be incomplete at redshift $z \gtrsim 0.6$ and masses $\log M_\star/\mathrm{M}_\odot \gtrsim 11.3$. The fibre diameter is of 2 arcsec. Velocity dispersions are determined in Thomas et al. (2013), using Penalized PiXel Fitting (PPXF; Cappellari & Emsellem 2004) and Gas AND Absorption Line Fitting algorithm (GANDALF; Sarzi et al. 2006) on the BOSS spectra. These values are quite robust being, on average, quite similar to the measurements from independent literature (see Thomas et al. 2013 for further details).

The final sample consists of 4118 MPA-JHU-DR7 galaxies and 5603 BOSS-DR10 galaxies, for a total of 9721 systems with structural parameters, spectroscopic redshifts and velocity dispersions. We limit to a mass-completed sample of galaxies with $\log M_\star/\mathrm{M}_\odot > 11.2$, consisting of a total of 3778 galaxies with redshift $0 < z < 0.7$.

In the following subsections we will provide more details about the products of the analysis of the KiDS data set and the dynamical procedure. In particular, in Section 2.2 we will describe how the structural parameters are determined. In Section 2.3 we will provide details about the derivation of the stellar masses, and the dynamical Jeans modelling is discussed in Section 2.4. In Section 2.5 we will define the total-to-stellar mass ratio and DM fraction. Finally, in Section 2.6 we discuss how progenitor bias is taken into account.

[1] The data catalogues are available from http://wwwmpa.mpa-garching.mpg.de/SDSS/DR7/raw_data.html

[2] The data catalogues are available from http://www.sdss3.org/dr10/spectro/galaxy_portsmouth.php

2.2 Structural parameters

Galaxy structural parameters have been derived via accurate 2D surface photometry of the highest S/N sample (La Barbera et al. 2008, 2010; Roy et al., in preparation). Surface photometry is performed using the 2DPHOT environment, an automatic computer code designed to obtain both integrated and surface photometry of galaxies in wide-field images. The software first produces a local point spread function (PSF) model from a series of identified *sure stars*. For each galaxy, this is done by fitting the four closest stars to that galaxy with a sum of three 2D Moffat functions. Then galaxy snapshots are fitted with PSF-convolved Sérsic models having elliptical isophotes plus a local background value (see La Barbera et al. 2008 for further details). The fit provides the following parameters for the four wavebands: surface brightness at R_e, μ_e, circularized effective radius, R_e, Sérsic index, n, total magnitude, m_S, axis ratio, q, and position angle. As it is common use in the literature, in this paper we use the circularized effective radius, R_e, defined as $R_\mathrm{e} = \sqrt{q}R_\mathrm{e,maj}$, where $R_\mathrm{e,\,maj}$ is the major-axis effective radius. For further details about the catalogue extraction and data analysis see Roy et al. (in preparation).

2.3 Stellar mass determination

To determine stellar masses, $M_\star$, we have used the software LE PHARE (Arnouts et al. 1999; Ilbert et al. 2006), which performs a χ^2 fitting method between the stellar population synthesis (SPS) theoretical models and data. Single burst models from Bruzual & Charlot (2003), with different metallicities ($0.2 \leq \mathrm{Z/Z}_\odot \leq 2.5$) and ages ($3 \leq \mathrm{age} \leq \mathrm{age}_\mathrm{max}$ Gyr), and a Chabrier (2001) IMF is used. The Salpeter (1955) gives masses larger of a factor ∼1.8 (Tortora et al. 2009; Swindle et al. 2011). The maximum age, $\mathrm{age}_\mathrm{max}$, is set by the age of the Universe at the redshift of the galaxy, with a maximum value at $z = 0$ of 13 Gyr. To minimize the probability of underestimating the stellar mass by obtaining too low an age, following Maraston et al. (2013) we have applied age cut-offs to the model templates, allowing for a minimum age of 3 Gyr. Models are redshifted using the SDSS spectroscopic redshifts. We adopt the observed KiDS *ugri* photometry (and related 1σ uncertainties) within a 6 arcsec aperture of diameter, corrected for Galactic extinction using the map in Schlafly & Finkbeiner (2011). Total magnitudes derived from the Sérsic fitting, m_S, are used to correct the outcomes of LE PHARE for missing flux. The single burst assumption and the older stellar populations and metal-richer models are suitable to describe the red and massive galaxies we are interested in (Gallazzi et al. 2005; Thomas et al. 2005; Tortora et al. 2009). Among LE PHARE outputs, we will adopt best-fitting masses in this paper.

2.4 Dynamical modelling

Following the analysis in Tortora et al. (2009, 2012) we model the SDSS aperture velocity dispersion of individual galaxies using the spherical isotropic Jeans equations to estimate the (total) dynamical mass M_dyn (which we will also refer to as M_tot) within $r = 1R_\mathrm{e}$. In the Jeans equations, the stellar density and the total mass distribution need to be specified. Thus, the stellar density is provided by the 2D Sérsic fit of the KiDS r-band galaxy images, and the total (DM+stars) mass is assumed to have the form of a singular

isothermal sphere (SIS), from which $M(r) \propto \sigma^2_{\rm SIS} r$ (corresponding to a 3D mass density slope $\gamma = 2$), where $\sigma_{\rm SIS}$ is the model (3D) velocity dispersion.

The total mass density profile in the centre of ETGs flattens with galaxy mass (Remus et al. 2013; Dutton & Treu 2014; Tortora et al. 2014b; Poci, Cappellari & McDermid 2017): low-mass ETGs have steep mass density distributions consistent with those of stars (i.e. consistently with a constant M/L profiles), while shallower isothermal profiles have been found to provide a robust description of the mass distribution in massive ETGs (e.g. Kochanek 1991; Bolton et al. 2006, 2008; Koopmans et al. 2006; Gavazzi et al. 2007; Auger et al. 2009, 2010; Chae, Bernardi & Kravtsov 2014; Oguri, Rusu & Falco 2014). This 'conspiracy' (Rusin, Kochanek & Keeton 2003; Treu & Koopmans 2004; Koopmans et al. 2006; Gavazzi et al. 2007; Tortora et al. 2009, 2014b; Auger et al. 2010) seems to be motivated also by theoretical arguments: an overall isothermal profile can be explained by a smaller amount of dissipation during the formation of such high-mass galaxies, if compared to lower mass systems, where higher level of dissipation leads to a more prominent contribution from newly formed stars to the total mass density in the centre, steepening their total density slope (Koopmans et al. 2006; Remus et al. 2013, 2017; Tortora et al. 2014b). For further details on the systematics introduced by the particular mass density profile choice, one can refer to Tortora et al. (2009, 2012) (see also Cardone et al. 2009, 2011; Cardone & Tortora 2010).

We will discuss the impact of a non-isothermal mass density profile and orbital anisotropy on our inferences in Section 4.3.

2.5 Dark matter content and rest-frame quantities

We characterize the mass content of an ETG by computing the deprojected total-to-stellar mass ratio $M_{\rm dyn}(r)/M_\star(r)$, i.e. the ratio between dynamical and stellar mass in a sphere of radius r and refer to the value assumed by this quantity at the effective radius $R_{\rm e}$, i.e. $M_{\rm dyn}(R_{\rm e})/M_\star(R_{\rm e})$, as the 'central' total-to-stellar mass ratio. As the total dynamical mass includes both stars and DM, we will also use a related quantity, which makes explicit the DM fraction within $R_{\rm e}$, defined as $f_{\rm DM}(R_{\rm e}) = 1 - M_\star(R_{\rm e})/M_{\rm dyn}(R_{\rm e})$. When not stated explicitly, $M_\star$ is referred to the SPS value assuming a Chabrier IMF, discussed in Section 2.3. Note that usually dynamical analysis formalisms include deprojected masses (e.g. see Tortora et al. 2009), while projected masses are typically present in strong lensing equations (e.g. Auger et al. 2010). The projected $M_{\rm dyn}/M_\star$ or $f_{\rm DM}$ are always larger than their deprojected versions within the same radius, because of the contribution of the outer parts of the halo along the line-of-sight.[3] In the following, we will discuss the DM quantities described above as a function of structural parameters, masses, velocity dispersion, stellar density and, mainly, as a function of the redshift.

In the spherical Jeans equation, for the stellar density we have adopted the observed r-band structural parameters, while $M_{\rm dyn}(R_{\rm e})/M_\star(R_{\rm e})$ are computed using rest-framed n and $R_{\rm e}$. Indeed, the effective radii should be referred to a fixed rest-frame wavelength to account for the effect of colour gradients, which make ETG optical $R_{\rm e}$ larger in bluer than in redder bands, on average. If this effect is not taken into account, then $R_{\rm e}$ are systematically larger at higher redshift (Sparks & Jorgensen 1993; Hyde & Bernardi 2009a; La Barbera & de Carvalho 2009; Roche, Bernardi & Hyde 2010; Beifiori et al. 2014; Tortora et al. 2014c; Vulcani et al. 2014). Similar considerations hold for the Sérsic indices. In particular, using a sample of galaxies with $z < 0.3$, Vulcani et al. (2014) estimate an increase from g to u and from r to g band of $\lesssim$15 per cent, and similar results are found in La Barbera & de Carvalho (2009) following the method in Sparks & Jorgensen (1993). We have determined the rest-frame structural parameters ($X = R_{\rm e}$ and n) by interpolating the observed X parameters in the three KiDS wavebands g, r and i. We have performed a linear fit,

$$\log X = a + b \log \lambda, \quad (1)$$

to the data points (λ_l, X_l), with $l = g, r, i$, where $\lambda_{g,\,r,\,i} = \{4735, 6287, 7551\}$ Å are the mean wavelengths of our filters. Then, we have assumed the g-band structural parameters at $z = 0$, $X(\lambda_g)$ in equation (1), and calculated the rest-frame g-band structural parameters at $z > 0$ as $X((1+z)\lambda_g)$. The average shifts with respect to the g-band quantities are -5 per cent for $R_{\rm e}$ and 7 per cent for n, with scatter of 50 and 40 per cent, respectively.

2.6 Progenitor bias

The results need to be corrected for progenitor bias, since low-z ETG samples contain galaxies that have stopped their star formation only recently and that would not be recognized as ETGs at higher redshifts. This is the case of systems with relatively young ages that cannot correspond to passive objects at higher z (van Dokkum & Franx 2001; Saglia et al. 2010; Valentinuzzi et al. 2010a,b; Beifiori et al. 2014; Tortora et al. 2014c).

The impact of the progenitor bias can push galaxy parameters in different directions, as discussed in Tortora et al. (2014c). For example the correlation of $R_{\rm e}$ with galaxy age is still controversial. In fact, contrasting results are found by observational analysis, which show that, at fixed mass or velocity dispersion, younger systems are larger (Shankar & Bernardi 2009; Napolitano et al. 2010; Tortora et al. 2010b; Valentinuzzi et al. 2010a) or are as sized as older galaxies (Graves, Faber & Schiavon 2009; Tortora et al. 2014c). The outcomes from semi-analytic galaxy formation models are also still unclear, as there are results showing that younger galaxies are larger (Khochfar & Silk 2006) or also smaller (Shankar et al. 2010) than the oldest systems.

To correct for the progenitor bias we would need an accurate estimate of the galaxy ages. Unfortunately our galaxy age have been obtained from the fitting of spectral models to our KiDS optical multiband photometry, hence they cannot be more than a qualitative guess. Thus, following Beifiori et al. (2014), we remove those galaxies whose age at redshift $z = 0.65$ – the centre of our highest redshift bin – was less than 3 Gyr, which is the time needed for a typical galaxy to become passive. This cut leaves 2595 galaxies, i.e. about 69 per cent of the total sample. In the rest of this paper, because of the uncertainties in our photometric ages, we will discuss both the results without and with this progenitor bias correction.

3 CORRELATION WITH STRUCTURAL PARAMETERS AND MASS PROBES

3.1 Dark matter fraction

Fig. 1 shows central $M_{\rm dyn}/M_\star$ as a function of different galaxy parameters, i.e. effective radius, Sérsic index, velocity dispersion,

[3] The projected stellar mass within $R_{\rm e}$ is $0.5M_\star$, while the deprojected stellar mass within the same radius is about $0.416M_\star$ (calculated using a Sérsic profile with $n = 4$). Instead, for a SIS, the projected mass is $\pi/2$ times the spherical mass, and this value is constant with radius. Therefore, the projected total-to-stellar mass ratio is $\sim$1.3 times (i.e. $\sim$0.12 dex) larger than the equivalent deprojected quantity.

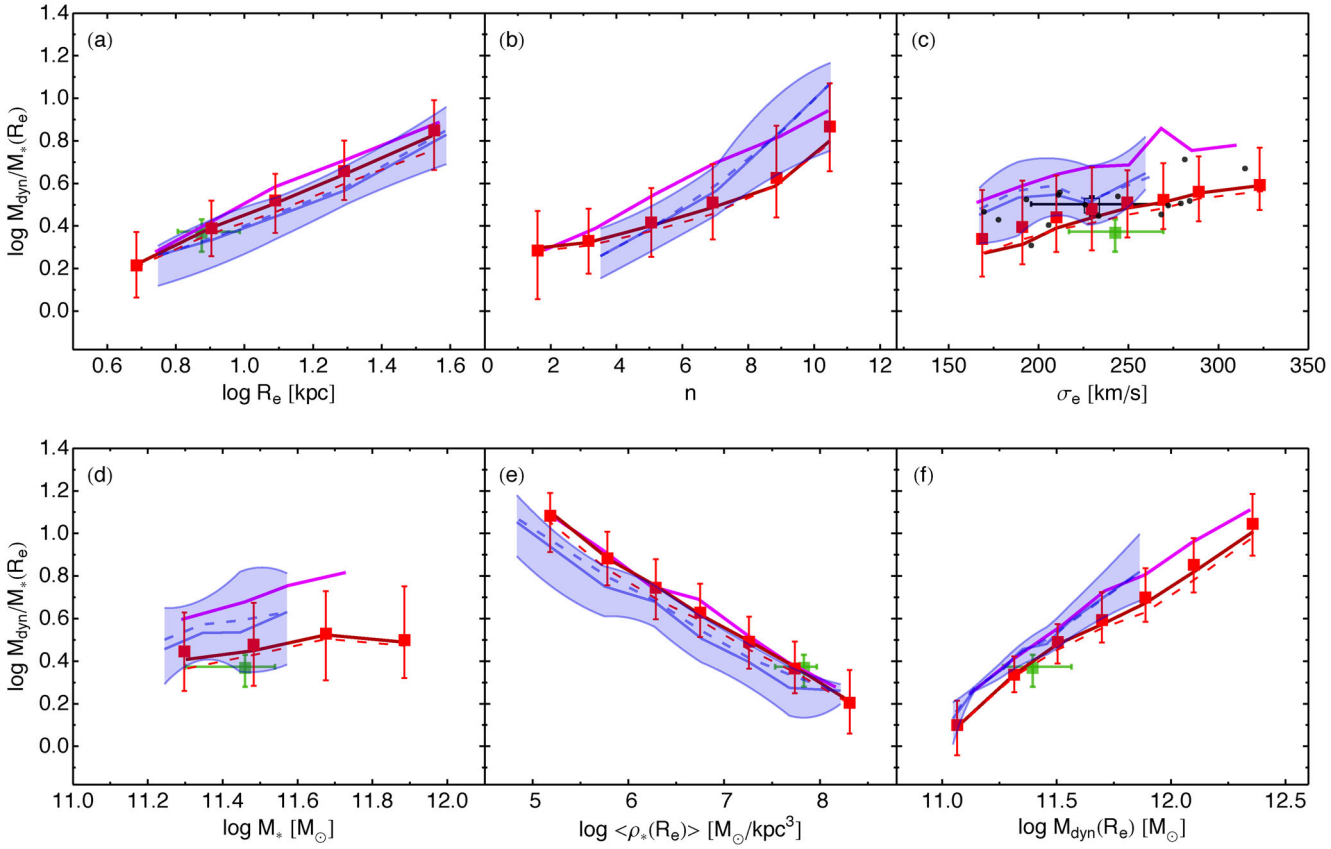

Figure 1. The total-to-stellar mass ratio $M_{\rm dyn}/M_\star$ within rest-frame effective radius, $R_{\rm e}$, assuming a Chabrier IMF, as a function of (a) rest-frame effective radius $R_{\rm e}$, (b) rest-frame Sérsic index n, (c) velocity dispersion within rest-frame effective radius $\sigma_{\rm e}$, (d) total stellar mass $M_\star$, (e) central average stellar density $\langle\rho_\star\rangle$ and (f) dynamical mass $M_{\rm dyn}$within rest-frame $R_{\rm e}$, $M_{\rm dyn}(R_{\rm e})$. The deprojected Sérsic law in the rest-frame g-band is used to describe the density profile of the stellar component. Red squares and error bars are medians and 25–75th percentile trends for the whole KiDS sample under analysis. Solid purple and dark red lines are medians for galaxies in the redshift bins $0.1 < z \leq 0.3$ and $0.3 < z \leq 0.7$. Dark blue line and light blue region are medians and 25–75th percentile trends for SPIDER galaxies with $M_\star > 10^{11.2}\,{\rm M}_\odot$. Dashed red (blue) lines are medians for results corrected for progenitor bias for KiDS (SPIDER) data sets. Green squares and error bars are medians and 25–75th percentiles for SLACS lenses from Auger et al. (2010). In panel (c), black dots, open square and error bars are single data points, median and 25–75th percentiles for the results in Thomas et al. (2011), which apply a Schwarzschild orbit superposition technique to a sample of 16 Coma ETGs.

stellar and dynamical mass and central average deprojected stellar density, $\langle\rho_\star\rangle$, defined as $\langle\rho_\star\rangle = M_\star(R_{\rm e})/(\frac{4}{3}\pi R_{\rm e}^3)$. Since here we have fixed the IMF to Chabrier, the $M_{\rm dyn}/M_\star$ trend implies a variation in the DM content. Red symbols are for the KiDS sample, where we have collected all the galaxies with redshift $z < 0.7$. Dashed blue lines with light blue shaded regions are for a sample of ETGs with redshifts $0.05 < z < 0.095$ from the SPIDER survey, assuming g-band structural parameters. Error bars and the shaded regions are the 25–75th percentiles. We will also fit the power-law relation $M_{\rm dyn}/M_\star \propto X^\alpha$, where X is one of the galaxy parameters ($R_{\rm e}$, n, $\sigma_{\rm e}$, $M_\star$, $\langle\rho_\star\rangle$, $M_{\rm dyn}$) and α is the slope of the correlation.[4] All the correlations are significant at more than 99 per cent.

We find a tight and positive correlation with a slope $\alpha = 0.72$ between $M_{\rm dyn}/M_\star$ and $R_{\rm e}$, which is interpreted as a physical aperture effect, where a larger $R_{\rm e}$ subtends a larger portion of a galaxy DM halo. A similar steep correlation also holds between $M_{\rm dyn}/M_\star$ and Sérsic index ($M_{\rm dyn}/M_\star \propto n^{0.62}$), which means that galaxies with steeper light profiles have higher central DM fractions. The galaxies with the smallest $R_{\rm e}$ (∼5 kpc) and Sérsic indices (∼2) have the smallest DM fraction (∼35 per cent), while the largest galaxies ($R_{\rm e} \sim 35$ kpc) with the steepest light profiles ($n \sim 10$) present the largest DM content (∼85 per cent).

We also find that $M_{\rm dyn}/M_\star$ correlates with $\sigma_{\rm e}$ ($M_{\rm dyn}/M_\star \propto \sigma_{\rm e}^{0.89}$). Galaxies with larger $M_{\rm dyn}$, i.e. with a larger content of both stellar and dark matter, have a larger DM content ($M_{\rm dyn}/M_\star \sim 10$, i.e. 90 per cent of DM), the slope of the correlation is 0.7. The correlation with $M_\star$ is shallower, with an average $M_{\rm dyn}/M_\star \sim 3$ (i.e. 67 per cent of DM) and $\alpha = 0.11$.

Fig. 1 also shows a sharp anticorrelation between DM content and central average stellar density with $\alpha = -0.28$, which has been reported for the first time in Tortora et al. (2012), and now is confirmed using samples of intermediate-redshift galaxies. Galaxies with denser stellar cores have lower DM fractions (i.e. $M_{\rm dyn}/M_\star \sim 2$ or $f_{\rm DM} \sim 0.5$ at $\rho_\star \sim \times 10^8\,{\rm M}_\odot\,{\rm kpc}^{-3}$), while $f_{\rm DM}$ values as high as ∼0.95 are found at the lowest densities ($\rho_\star \sim 10^5\,{\rm M}_\odot\,{\rm kpc}^{-3}$). This trend results from the fact that, on average, higher stellar densities correspond to smaller effective radii, implying a lower $M_{\rm dyn}/M_\star$. All these trends are qualitatively consistent with those found for a sample of massive $z \sim 0$ SPIDER galaxies (blue lines with shaded regions; see also Tortora et al. 2012). Our results

[4] The $\sigma_{\rm e}$ is the SDSS-fibre velocity dispersion, $\sigma_{\rm Ap}$, corrected to an aperture of $1R_{\rm e}$, following Cappellari et al. (2006).

confirm most of the previous literature at $z \sim 0$ (e.g. Padmanabhan et al. 2004; Cappellari et al. 2006; Hyde & Bernardi 2009a; Tortora et al. 2009, 2012; Napolitano et al. 2010), or at intermediate redshift (Auger et al. 2010; Tortora et al. 2010b,c).

In Fig. 1 we also plot the results when progenitor bias is accounted for (dashed lines), showing that the trends are almost unaffected. We have finally plotted the results for two redshift bins: $0.1 < z \leq 0.3$ (purple solid line) and $0.3 < z \leq 0.7$ (darker red line). Excepted for the correlations with R_e and $\langle\rho_\star\rangle$, we find an evolution in the $M_{dyn}/M_\star$, with larger DM fraction in the lower redshift bin. Note that the median $M_{dyn}/M_\star$ of the $z \sim 0$ SPIDER galaxies are smaller than those of KiDS galaxies in the lower redshift bin with $0.1 < z \leq 0.3$. This seems to contract the trend of higher $M_{dyn}/M_\star$ at lower redshift just discussed and shown in Fig. 1. However, we caution the reader that this discrepancy can arise from differences in the sample selection and the analysis of the data sets, as such as the determination of stellar masses, which are determined using different apertures for magnitudes, sets of filters and spectral templates (see Section 4.3 for further details). We will come back to the dependence on the redshift in Section 4.

We have also compared our results with $M_{dyn}/M_\star$ estimates from gravitational lensing and velocity dispersion of Sloan Lens ACS (SLACS) lenses (Auger et al. 2009, 2010). We have taken lenses with $\log M_\star/M_\odot > 11.2$ and an average redshift of $z \sim 0.2$. Lensing data needed to be homogenized in order to be compared with our $M_{dyn}/M_\star$ values in Fig. 1, specifically by (a) converting their size and stellar mass estimates to our cosmology, (b) extrapolating masses from $R_e/2$ to $1R_e$ and finally (c) deprojecting both stellar and dynamical mass within R_e. To do that we have adopted for simplicity a SIS model, which is on average a good approximation of their best-fitting total mass density, since their fitted power-law models are peaked around an isothermal slope. Lensing homogenized medians and 25–75th percentiles are shown with green symbols in Fig. 1. An agreement is found for the $M_{dyn}/M_\star$–R_e and $M_{dyn}/M_\star$–$\langle\rho_\star\rangle$, while we notice that at fixed $M_\star$, σ_e and M_{dyn}, SLACS $M_{dyn}/M_\star$ are smaller of $\sim$0.3 dex than the lower z KIDS relation (purple lines). However, at fixed $M_\star$, the SLACS sizes are smaller than the ones of the KiDS sample by $\sim$0.15 dex, while velocity dispersions are higher of $\sim$0.03 dex, which implies than that SLACS M_{dyn} and $M_{dyn}/M_\star$ are smaller of $\sim$0.1 dex within their R_e. The smaller sizes of SLACS galaxies are also clear from the $M_{dyn}/M_\star$–R_e and $M_{dyn}/M_\star$–$\langle\rho_\star\rangle$ correlations, where SLACS galaxies have sizes concentrated towards smaller values, with respect to the range of sizes of SPIDER and KiDS data samples. The origin of these discrepancy on sizes of galaxies of similar stellar mass can reside on the assumption of a de Vaucouleurs (1948) profile adopted by Auger et al. (2009) for their surface photometry fit. It is known that larger Sérsic n values (typical of massive ETGs) produce R_es that are larger of the de Vaucouleurs values of $\sim$0.2 dex or more (Tortora et al. 2012).

In panel (c) of Fig. 1 we also plot the results from the Thomas et al. (2011), which make use of Schwarzschild orbit superposition models in axisymmetric potentials to a sample of 16 Coma ETGs. We consider their results for a mass-follows-light model and calculate the $M_{dyn}/M_\star$ from their table 1, dividing the best-fitting dynamical M/L to the Kroupa IMF stellar M/L (converted to a Chabrier IMF). Furthermore, for a fair comparison with our SIS-based results, we have re-scaled their $M_{dyn}/M_\star$ using the average ratio of the virial factors for SIS and constant M/L profile estimated in Tortora et al. (2012). These results are shown as black dots, and medians with 25–75th percentiles are plotted as black square with error bars. The results are consistent with SPIDER, but $\sim$0.2 dex smaller than lower z KiDS values. However, as for SLACS lenses, the effective radii adopted by Thomas et al. (2011), have been obtained fitting a de Vaucouleurs profile (Jorgensen, Franx & Kjaergaard 1995; Mehlert et al. 2000), which can be again the reason of the observed discrepancy as their underestimated R_e might have produced smaller $M_{dyn}/M_\star$.

Our derivation of f_{DM} yields some cases where galaxies have unphysical $f_{DM} < 0$, since $M_{dyn}(R_e) < M_\star(R_e)$. We find that only $\sim$6 per cent of our galaxies have negative DM fractions. Using a Salpeter IMF we would have obtained smaller DM fraction, and for $\sim$23 per cent even negative. We also find that these numbers are changing with redshift, with $\sim$1, 3 and 12 per cent of negative f_{DM} in the redshift bins $0.1 < z \leq 0.3$, $0.3 < z \leq 0.5$ and $0.5 < z \leq 0.7$. These fractions translate to $\sim$5, 18 and 34 if a Salpeter IMF is adopted. This is a well-known critical effect also discussed in previous works (see e.g. Tortora et al. 2009, 2012; Napolitano et al. 2010). However, although a fraction or almost all of these negative f_{DM} could be compatible with observational scatter in $M_\star$ and M_{dyn} (see Napolitano et al. 2010), it does not leave a complete freedom on the assumption of the IMF to adopt. In particular, higher stellar M/L normalizations are unphysical for those systems that tend to have smaller f_{DM} (e.g. the ones with smaller sizes and dynamical masses, larger stellar densities, higher redshift, etc.). In principle, one can ask whether by releasing the concept of the universal IMF it is possible to interpret all the trends of the mass excess in the central regions with a stellar mass excess (i.e. an IMF variation) rather than DM excess (i.e. f_{DM} variation) with galaxy parameters as in Fig. 1 (e.g. Tortora et al. 2009, 2012, 2013; Spiniello's thesis, chap. 2).

3.2 Constraining the IMF

In this section we want to consider the case of a non-universal IMF and correlate the IMF variation with galaxy parameters. The IMF has been initially considered as universal across galaxy types and cosmic time, mostly because of a lack of evidence of variations among stellar clusters and OB associations in the Milky Way (see Bastian, Covey & Meyer 2010, for a review about IMF studies). This assumption has been recently questioned by different dynamical, lensing and stellar population studies, finding evidence for systematic IMF variations in ETGs (Treu et al. 2010; Thomas et al. 2011; Cappellari et al. 2012, 2013; Conroy & van Dokkum 2012; Spiniello et al. 2012; Wegner et al. 2012; Dutton et al. 2013; Ferreras et al. 2013; Goudfrooij & Kruijssen 2013, 2014; La Barbera et al. 2013; Tortora et al. 2013, 2014a,b, 2016; Weidner et al. 2013; Martín-Navarro et al. 2015; Shu et al. 2015; Lyubenova et al. 2016; Corsini et al. 2017; Li et al. 2017; Sonnenfeld et al. 2017).

Following Tortora et al. (2012) and motivated by all the results pointing to a non-universal IMF (see in particular Tortora et al. 2014b), we can check how large the IMF has to be to cancel the presence of DM within $1R_e$. We estimate the expected variation of stellar mass normalization, defining the mismatch parameter $\delta_{IMF} \equiv M_{\star,IMF}(R_e)/M_\star(R_e)$, relative to a Chabrier IMF, where $M_\star$ is the stellar mass estimated with a Chabrier IMF and $M_{\star,IMF}$ is the stellar mass for any other IMF assumption. We can also define the related DM fraction as the one obtained for the particular IMF assumed, i.e. $f_{DM} = 1 - M_{\star,IMF}(R_e)/M_{dyn}(R_e)$. The estimated δ_{IMF} with the assumption $f_{DM} = 0$ is substantially the $M_{dyn}/M_\star$ plotted in Fig. 1, but with $M_{dyn} = M_{\star,IMF}$. The IMF mismatch parameter corresponding to $f_{DM} = 0$ represents an extreme upper limit, since in the ΛCDM a non-zero DM fraction is found also when accounting for a non-universal IMF (see e.g. Cappellari et al. 2013; Tortora

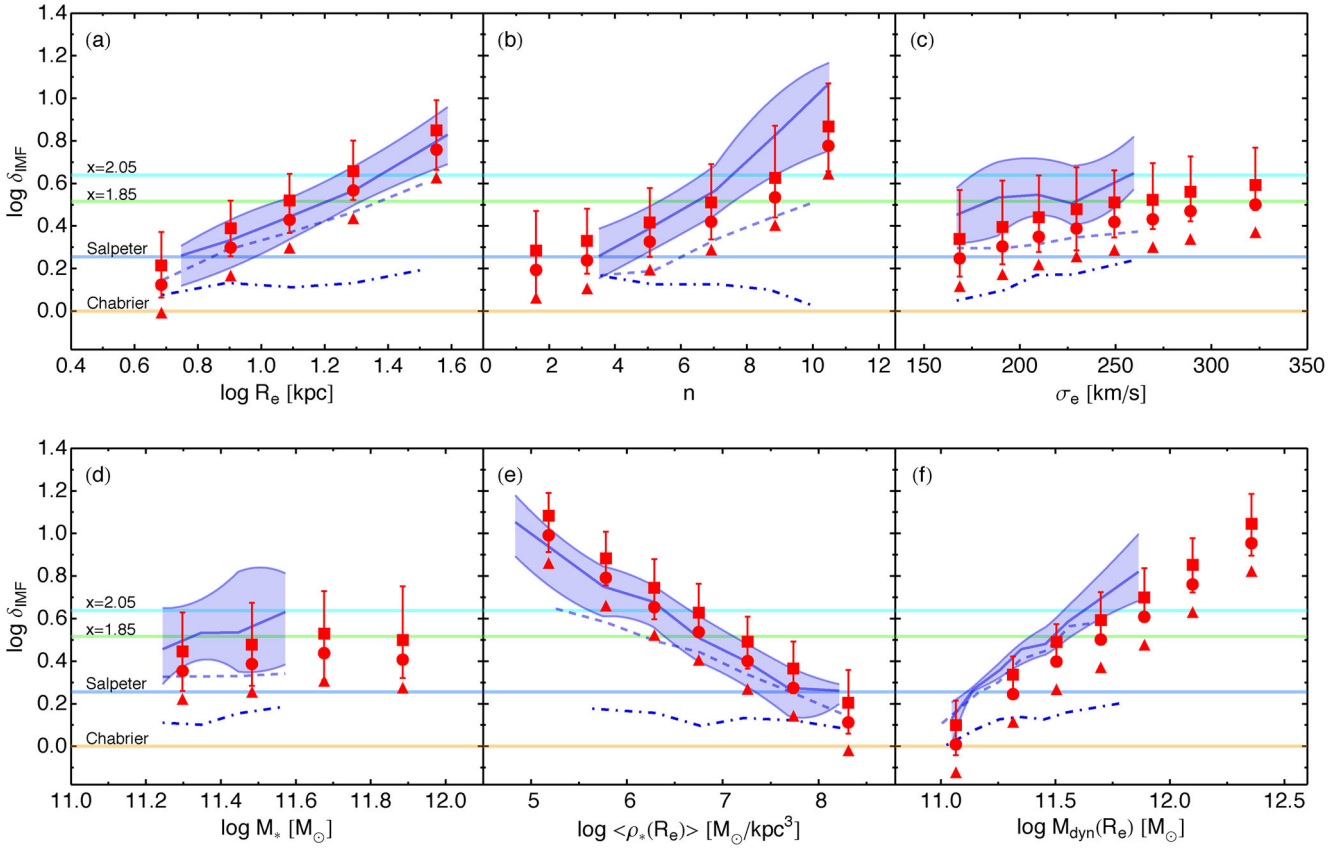

Figure 2. Trends of the mismatch parameter δ_{IMF} as a function of (a) effective radius R_e, (b) Sérsic index n, (c) velocity dispersion within effective radius σ_e, (d) total stellar mass $M_\star$, (e) central average stellar density $\langle\rho_\star\rangle$ and (f) dynamical mass M_{dyn}within R_e, $M_{dyn}(R_e)$. R_e and n are rest-frame quantities. The filled red squares with bars are medians and 25–75th percentiles for a SIS profile assuming a null DM fraction within R_e. Filled circles and triangles correspond to the medians adopting a SIS profile with 20 and 40 per cent of DM within R_e, respectively. DM fraction in the non-universal IMF framework is defined as $f_{DM} = 1 - M_{\star,IMF}(R_e)/M_{dyn}(R_e)$. Dark blue lines and light blue regions are medians and 25–75th percentile trends for SPIDER galaxies with $M_\star > 10^{11.2}\,M_\odot$. Horizontal lines correspond to the relative variation of stellar mass, $M_{\star,IMF}/M_\star$ – with respect to a Chabrier IMF – when adopting synthetic models with different IMFs, with slopes 1.35 (i.e. a Salpeter IMF; blue), 1.85 (green) and 2.05 (cyan). And the orange line corresponds to the case of a Chabrier IMF ($M_{\star,IMF} = M_\star$). For completeness and to study systematics in the trends, we have also plotted the results for the SPIDER sample using K_s-band profile (short-dashed blue line). The point-dashed blue line is for the NFW+star model with variable stellar M/L in Tortora et al. (2014b).

et al. 2013). Hence, to explore more realistic DM fractions, we have also computed the IMF mismatch corresponding to $f_{DM} = 0.2$ or $f_{DM} = 0.4$, which bracket the typical values of the DM fraction found in SPIDER ETGs, when a free IMF normalization is adopted (Tortora et al. 2013). By construction, for the $f_{DM} = 0.2$ and 0.4 cases, our $M_{dyn}/M_\star$ give a mass budget in stars, and thus δ_{IMF} values, which are systematically lower than the $f_{DM} = 0$ case.

To derive inferences about the IMF slope, we compare this dynamical δ_{IMF} with what is expected from stellar population models. Thus, we consider three power-law IMFs, with slopes 1.35 (i.e. Salpeter), 1.85 and 2.05 (i.e. a very bottom-heavy IMF). The δ_{IMF} is estimated as the ratio of the stellar M/L between two simple stellar populations (SSPs) having a power law and a Chabrier IMFs, respectively. We compute the stellar K-band M/L, adopting the Bruzual & Charlot (2003) synthesis code, for old (10 Gyr) SSPs, with solar metallicity (see Tortora et al. 2012).

Fig. 2 plots the δ_{IMF} trends, for three different assumptions of the DM fraction, as a function of R_e, n, σ_e, $M_\star$, $\langle\rho_\star\rangle$ and M_{dyn} (red symbols). We compare the results against the $z \sim 0$ estimate from SPIDER for f_{DM}=0. Horizontal lines mark δ_{IMF} for the different IMFs obtained from stellar population synthesis. The intersections with the horizontal lines define the values of R_e, n, σ_e, $M_\star$, $\langle\rho_\star\rangle$ and M_{dyn} for which a given IMF slope would imply $f_{DM} = 0$, 0.2 and 0.4.

The figure shows that, in order to account for the apparent trend of f_{DM} with R_e, n, $\langle\rho_\star\rangle$ and M_{dyn}, galaxies with the largest radii, Sérsic indices and dynamical masses and the lowest $\langle\rho_\star\rangle$ should have an IMF slope as steep as (or steeper than) 2.05 (e.g. Tortora et al. 2013, 2014b; Spiniello et al. 2015). While at the lowest values of R_e, n and M_{dyn}, and highest $\langle\rho_\star\rangle$, a Salpeter (Chabrier) IMF would be required if $f_{DM} = 0$ ($f_{DM} = 0.4$). Interestingly, in our mass range, δ_{IMF} is almost constant with stellar mass and is consistent with a slope $\sim$1.8 when $f_{DM} = 0$, and with a Salpeter IMF if $f_{DM} =$ 0.4. Despite the adopted constant f_{DM}, the trends with the parameters remain qualitatively the same and just shifted towards a lower normalization for higher f_{DM} values.

However, IMFs with slopes $x \gtrsim 2$ are disfavoured in SLACS gravitational lenses, since they give stellar M/Ls that violate the total mass inside the Einstein radius, i.e. within $\sim R_e/2$ (Spiniello et al. 2012). Thus, the assumption of no DM within R_e is not realistic and would be at odds with other results using gravitational lensing, too (see also later on in this paper).

Before starting to drive conclusions, we need to check how our assumptions might affect the main results of our analysis. All

sources of systematics will be discussed in Section 4.3, however here we start showing the effect of unaccounted colour gradients and the galaxy model, using the SPIDER sample. For this sample we show the *K*-band results as dashed blue lines in Fig. 2, which provide smaller $\delta_{\rm IMF}$ of about 0.2 dex, but with trends that are almost unchanged. We also plot the best-fitting $\delta_{\rm IMF}$ derived in Tortora et al. (2014b), using a standard NFW for the DM halo and a *K*-band light profile (dot–dashed blue line). The differences among these two results are naturally explained by the fact that dashed blue lines assume a SIS profile for the total mass distribution and $f_{\rm DM} = 0$, while point-dashed blue lines correspond to a NFW plus light model, which also predict non-zero DM fractions (Tortora et al. 2013, 2014b).

4 EVOLUTION WITH REDSHIFT

A simple monolithic-like scenario, where the bulk of the stars is formed in a single dissipative event followed by a passive evolution, is no longer supported by the observations, while many observations suggest the occurrence of a strong mass and size evolution in ETGs (Daddi et al. 2005; Trujillo et al. 2006, 2007; Saglia et al. 2010; Trujillo, Ferreras & de La Rosa 2011; Tortora et al. 2014c). In this section, we will first investigate the evolution of size and DM fraction as a function of redshift, at fixed stellar mass, comparing the results with some literature and predictions from different galaxy evolution scenarios. Then, to study in more detail the evolution of the mass and size in our galaxy sample, we compare some relevant correlations, as the ones between the galaxy size or DM fraction and $M_\star$, at different redshifts (Tortora et al. 2014c). In this latter case, we will create some toy models to interpret this evolution in terms of physical processes.

Previous analyses addressing the DM fraction evolution with redshift (e.g. Tortora et al. 2014c based on the EDisCS sample and Beifiori et al. 2014 based on BOSS) have shown that ETGs contain less DM within the effective radius at larger redshift. In this paper, we will complement our analysis in Tortora et al. (2014c), determining the DM evolution self-consistently, i.e. using the same data sample processed with exactly the same analysis.

4.1 Evolution at fixed mass

Following some previous studies about size and velocity dispersion evolution we investigate how $R_{\rm e}$, $\sigma_{\rm e}$ and $M_{\rm dyn}/M_\star$ change in terms of redshift, at fixed stellar mass. We concentrate our attention on two particular stellar mass bins ($11.2 < \log M_\star/{\rm M}_\odot \leq 11.4$ and $11.4 < \log M_\star/{\rm M}_\odot \leq 11.6$). Almost all the correlations discussed are significant at more than 99 per cent. In Fig. 3 we first plot the dependence of $R_{\rm e}$ with the redshift (panels a and b), which shows that sizes were smaller at earlier epochs of galaxy evolution (see Roy et al., in preparation, for further details about size evolution in KiDS galaxies). Following a standard approach in the literature, we fit the relation $R_{\rm e} = R_{\rm e,0}(1+z)^\alpha$ to the data. For the two mass bins, in the case of no progenitor bias correction (red filled squares with error bars), we find a slope, $\alpha = -2.2$ and -3.8, respectively. These values translate into a weaker size evolution if we account for the progenitor bias (open squares with dashed red lines): in fact, the slopes become $\alpha = -1.6$ and -3.3 in this case. These trends are steeper than the trends for spheroid- and disc-like systems with $M_\star > 10^{11}\,{\rm M}_\odot$ taken from the literature (solid and dashed black lines in the top panels in Fig. 3; Trujillo et al. 2007; Buitrago et al. 2008; Conselice 2014). At lower z we find a good agreement with the $R_{\rm e}$s from SPIDER data sample. However, we find some discrepancy in the size normalization with other analysis. For example, the *I*-band measurements from EDisCS sample (Saglia et al. 2000; Tortora et al. 2014c) are lower of ∼0.3 dex, while the *i*-band $R_{\rm e}$ in Beifiori et al. (2014),[5] re-calibrated using *Hubble Space Telescope* (*HST*) images, are smaller of a factor of ∼0.2 dex. The difference in the wavebands adopted (*i*-band $R_{\rm e}$ in Beifiori et al. 2014 versus our rest-frame $R_{\rm e}$) cannot account for the observed large discrepancy. Overall, our results confirm the well-known result that in massive galaxies the size of the galaxies is changing with redshift (Daddi et al. 2005; Trujillo et al. 2006, 2007; Buitrago et al. 2008; van der Wel et al. 2008).

In panels (c) and (d) of Fig. 3 we also plot the effective velocity dispersion, $\sigma_{\rm e}$, as a function of the redshift. In this case the evolution with redshift is shallower, with higher z galaxies having slightly larger velocity dispersions (Cenarro & Trujillo 2009; Posti et al. 2014). In this case the evolution of $\sigma_{\rm e}$ is quantified through the relation $\sigma_{\rm e} = \sigma_{\rm e,0}(1+z)^\alpha$ where the estimated slopes for the two mass bins above are $\alpha = 0.21$ and 0.53 (without progenitor bias) and $\alpha = 0.46$ and 0.53 (with progenitor bias), respectively. These results are in good agreement with local (La Barbera et al. 2010; Tortora et al. 2012), intermediate-z (Beifiori et al. 2014) and higher z (Saglia et al. 2010; Tortora et al. 2014c) measures.

The total-to-stellar mass ratio (with a Chabrier IMF) is plotted in panels (e) and (f) of Fig. 3. The galaxies are DM dominated at lower redshift (i.e. 75–80 per cent of DM at $z \sim 0.2$), while $f_{\rm DM}$ results to be smaller at higher z (40–50 per cent at $z \sim 0.6$). Fitting the $M_{\rm dyn}/M_\star = (M_{\rm dyn}/M_\star)_0(1+z)^\alpha$ relation to the data, for the two mass bins we find $\alpha = -2.4$ and -2.8 (without progenitor bias) and $\alpha = -1.3$ and -2.2 (with progenitor bias), respectively. We find a small discrepancy with SPIDER and EDisCS data sample, but these results agree within the data scatter. We also plot the $M_{\rm dyn}/M_\star$ derived in Beifiori et al. (2014), assuming a non-homologous constant M/L profile (with SDSS sizes recalibrated to *HST* values) as a dashed cyan line. This latter model cannot be directly compared to our results because of its different assumption on the total mass distribution, hence we have rescaled their $M_{\rm dyn}/M_\star$ using the average ratio of the virial factors for SIS and constant M/L profile estimated in Tortora et al. (2012). After this renormalization (solid cyan line in Fig. 3) the Beifiori et al. (2014) estimates are on average consistent within $1\,\sigma$ scatter with the KiDS sample.

We want to interpret the trends of $\sigma_{\rm e}$ and $M_{\rm dyn}/M_\star$ in the context of galaxy evolution, by comparing the observed trends with the predictions from two different scenarios invoked to explain the galaxy size evolution. The merging scenario (MS, hereafter) predicts that size is driven by the accretion of matter, with the result that the sizes of the merger remnants are larger than those of their remnants. The merging model of Hopkins et al. (2009) predicts that the velocity dispersion varies in terms of the size as $\sigma_\star(z) \propto (1+\gamma)^{-1/2}\sqrt{\gamma + R_{\rm e}(0)/R_{\rm e}(z)}$, where the parameter γ sets the DM contribution to the potential relative to that of the baryonic mass. This parameter varies between 1 and 2 (which are the best-fitting values for $M_\star \sim 10^{11}$ and $\sim 10^{12}\,{\rm M}_\odot$, respectively). Completely different is the 'puffing-up' scenario (PS, hereafter) from Fan et al. (2008), which predicts that galaxies grow by the effect of quasar feedback, which removes huge amounts of cold gas from the central regions, quenching the star formation and increasing the size of the galaxy. This model predicts that velocity dispersion varies as $R_{\rm e}^{-1/2}$.

[5] Note that the mass range used by Beifiori et al. (2014) is not exactly the same of the first mass bin, used in this paper.

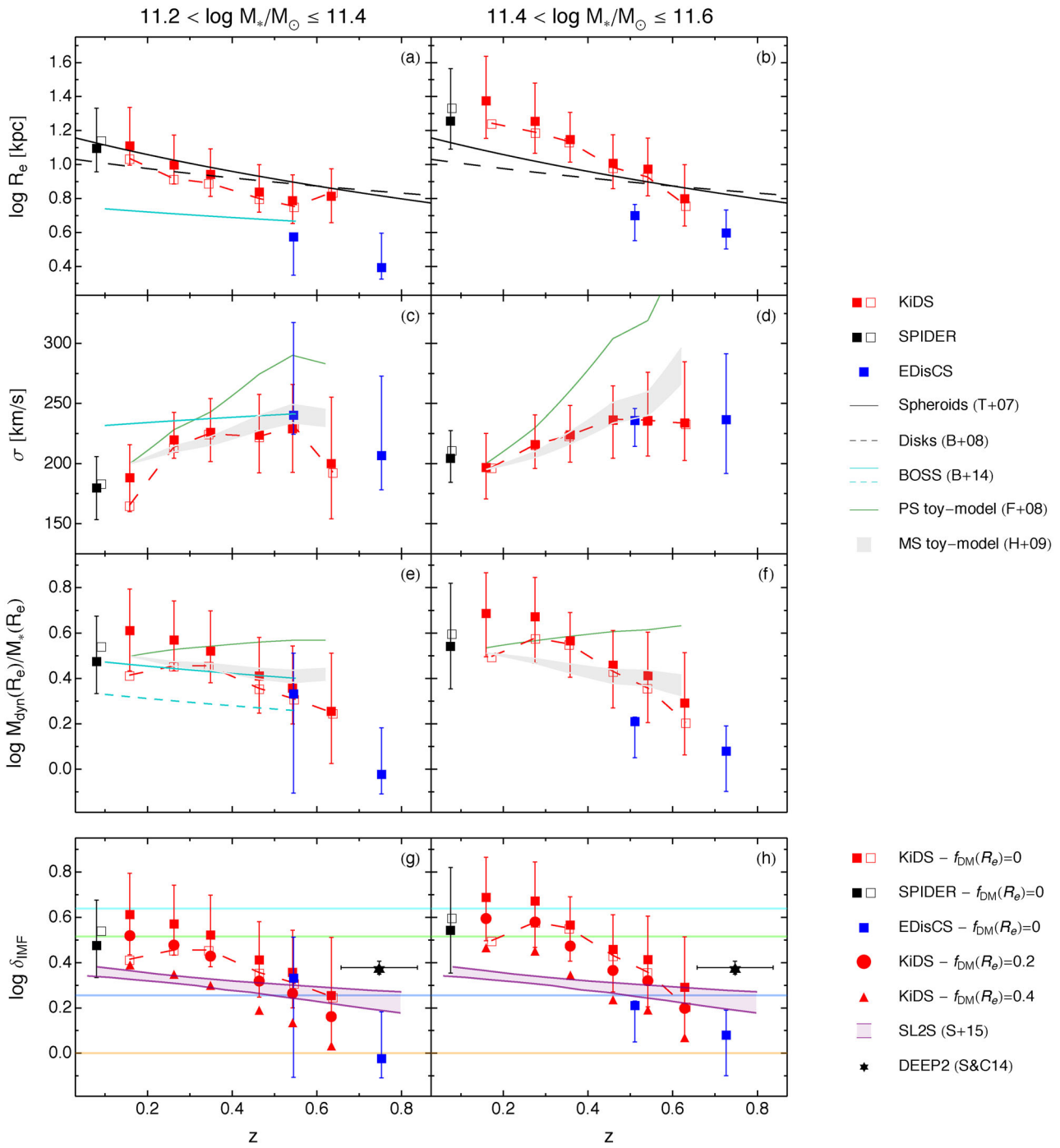

Figure 3. Evolution with redshift of R_e (panels a and b), σ_e (panels c and d), $M_{dyn}/M_\star$ (panels e and f) and δ_{IMF} (panels g and h) for two stellar mass bins: $11.2 < \log M_\star/M_\odot \leq 11.4$ (left) and $11.4 < \log M_\star/M_\odot \leq 11.6$ (right). Red symbols are as in previous figures. Open black square with error bar is median and 25–75th percentiles for SPIDER galaxies, while open black square is the median for the SPIDER sample when the progenitor bias is taken into account. Blue squares with bars are median and 25–75th percentiles for EDisCS sample. Cyan solid lines in panels (a), (c) and (e) are from Beifiori et al. (2014, B+14). In panel (e) the dashed line is calculated converting the results in Beifiori et al. (2014) assuming a constant M/L profile to a SIS profile, as explained in the text. The black solid and dashed lines in the top panels are taken from the average $R_e/R_{e,0}$–z trends (with $R_{e,0} = R_e(z \sim 0)$) for spheroid-like galaxies in Trujillo et al. (2007, T+07) and disc-like systems in Buitrago et al. (2008, B+08), normalized to $R_{e,0} = 15$ and 11 kpc, respectively. Shaded grey region and green line are our predictions using the merging model of Hopkins et al. (2009, H+09) and the 'puffing-up' scenario from Fan et al. (2008, F+08), respectively. See the text for further details. In the bottom panels (g and h), we show the δ_{IMF} when $f_{DM} = 0$ (filled squares) $f_{DM} = 0.2$ (filled circles) and $f_{DM} = 0.4$ (filled triangles), as in Fig. 2. Purple lines and shaded regions are the results obtained from the strong lensing and dynamical analysis of 80 ETGs in Sonnenfeld et al. (2015, S+15) and Sonnenfeld et al. (2017), the region sets the 68 per cent confidence level. The black star with error bars is for the average δ_{IMF} obtained by analysing the kinematical data of a sample of 68 galaxies at $z \sim 0.75$ in Shetty & Cappellari (2014, S&C14). Horizontal lines correspond to the relative variation of stellar mass, $M_{\star,IMF}/M_\star$ – with respect to a Chabrier IMF – as in Fig. 2. See legend at right, explanation in the main text and the text in this caption for abbreviations.

To derive predictions in the above scenarios, we use as R_e–z relation the interpolating line going through the KiDS median values in panels (a) and (b) of Fig. 3. This latter is inserted into the two equations discussed to derive the predicted velocity dispersions in the two schemes. Then we need to translate these predicted velocity dispersions into a $M_{dyn}/M_\star$. In order to do this we need first to derive the M_{dyn} as a function of the redshift, solving the spherical Jeans equation, which contains (1) the density of the light distribution, (2) the total potential and (3) all as a function of redshift. For the light distribution we have taken the Sérsic profile with $n = 4$ for simplicity (i.e. a pure de Vaucouleurs) and with effective radius given by our interpolated $R_e(z)$ relation as defined above. For the total potential we have used the SIS profile. Then, we impose that the velocity dispersion derived from Jeans equation (averaged within R_e) equals the $\sigma(z)$ in the two scenarios, MS and PS. This procedure provides M_{dyn} and $M_{dyn}/M_\star$ as a function of redshift. Note that what is relevant in this calculation is the trend with redshift and not the normalization, which is fixed by hand, since in the $\sigma_\star(z)$ formulae the normalization factor is unspecified.

We plot the predicted trends for σ_e and $M_{dyn}/M_\star$ in panels (c)–(f) of Fig. 3. The PS predicts a very strong evolution (with a change of $\sim$100 km s^{-1} in the redshift window analysed), which is discrepant with KiDS results for both the σ_e and $M_{dyn}/M_\star$. On the contrary, the milder evolution from MS accommodates the observations. See a similar analysis for the σ evolution in Cenarro & Trujillo (2009), where similar conclusions are reached. However, while the agreement with the velocity dispersion seems very good, the model predicts a shallower $M_{dyn}/M_\star$–z trend than the observed one, in both the mass bins.

Following the analysis made in Section 3, in panels (g) and (h) of Fig. 3 we also interpret the evolution of the $M_{dyn}/M_\star$ with redshift in terms of a change in the IMF and of DM content. We show how the mismatch parameter δ_{IMF} is changing in terms of redshift, for three different f_{DM} values ($f_{DM} = 0$, 0.2 and 0.4). If we assume that $f_{DM}(R_e)$ is not changing with redshift, then the observed $M_{dyn}/M_\star$ evolution can be explained by a change of the IMF 'normalization'. The δ_{IMF} values found for $f_{DM} = 0$ need to be considered as upper limits, and point to a Salpeter IMF at $z \sim 0.65$ and a very steep IMF at low redshift (with $x \sim 2.05$), if $f_{DM} = 0$. For the maximal DM fraction adopted here, i.e. $f_{DM} = 0.4$, KiDS results suggest a standard Chabrier IMF at $z \sim 0.65$ and slightly super-Salpeter at $z \sim 0$. If we consider that a more realistic situation would allow for a variation of f_{DM} with redshift (e.g. from $f_{DM} = 0$ at $z \sim 0.65$ to $f_{DM} = 0.4$ at $z \sim 0$), then the δ_{IMF} evolution would result weaker or totally absent.

We finally compare our findings for δ_{IMF} with some results from the literature. Sonnenfeld et al. (2015, 2017) measure δ_{IMF} for a sample of 80 massive ETGs, using strong lensing and velocity dispersion data. We plot their 68 per cent confidence region with purple symbols in Fig. 3. Their trend is shallower than our results found assuming a constant f_{DM} value. An agreement with these results can be found if we allow in our data for the more realistic f_{DM} evolution discussed above, i.e. if we assume that f_{DM} is null at $z \sim 0.65$ and $\gtrsim 0.4$ at $z \sim 0$. The black star with error bars is the average δ_{IMF} from Shetty & Cappellari (2014), obtained through the dynamical modelling of kinematical data of a sample of 68 massive ($M_\star \gtrsim 10^{11}$ M$_\odot$) galaxies at $z \sim 0.75$, extracted from the Deep Extragalactic Evolutionary Probe 2 (DEEP2) spectrographic survey. As in our $f_{DM} = 0$ case, their results have to be considered as upper limits, since they assume that mass follows light and no DM at all is considered. Their estimate would be normalized to our mass model assumption. This would be done by adding a factor $\sim$0.14 dex to covert a constant M/L profile to a SIS (Tortora et al. 2012), but their value would be larger of $\sim$0.16 dex if compared with the virial estimator, which they suggest to be related to underestimated R_e in the virial estimator formula (see Cappellari et al. 2013; Shetty & Cappellari 2014). Thus, since these two factors would almost elide, we have decided to not add any corrective factor to their δ_{IMF} estimate shown in Fig. 3. These results are about 0.1 dex larger than our $f_{DM} = 0$ findings at the same redshifts (see KiDS and EDisCS data points in Fig. 3).

As it has been done for the central DM evolution presented in panels (e) and (f) of Fig. 3, it would be interesting to interpret if this change of IMF with time is realistic and if is consistent with specific processes. In Tortora et al. (2014c) we proposed some speculative considerations, suggesting that a change of IMF with redshift could be produced by two different processes: (a) new stars formed in the galaxy centre during a wet merging process, which also produce 'higher mass' IMF (Napolitano et al. 2010) and positive age gradients (Tortora et al. 2010a) in young and massive local ETGs, or (b) by stars from both merging galaxies, which are characterized by two different IMFs, which can combine to modify the cumulative IMF of the merger remnant. Unfortunately, the net effect of these processes on the final IMF normalization is not yet clear, and in most cases the combination of a 'higher' and a 'lower' mass IMF would produce a diluted IMF. Thus, galaxy mergers would produce smaller δ_{IMF} values, or leave δ_{IMF} almost constant with redshift, as predicted by the galaxy merging toy models in Sonnenfeld et al. (2017). These results contrast the strong evolution observed in panels (g) and (h) of Fig. 3.

All these results seem to suggest that most of the $M_{dyn}/M_\star$ evolution would be driven by a change of the DM fraction. A deeper analysis will be needed to constrain the IMF and DM fraction in term of redshift. In a future paper we will discuss this problem with more details.

4.2 Size, mass and DM evolution

The analysis performed in the previous section cannot be conclusive, since it does not take into account that in merging processes a single galaxy also changes in mass. For this reason, in Fig. 4 we compare the R_e–$M_\star$ and $M_{dyn}/M_\star$–$M_\star$ relations (assuming a fixed Chabrier IMF) for KiDS galaxies at different redshift and study the joint evolution of size and mass. We start seeing how lower redshift galaxies are larger and contain more DM in their cores at all values of $M_\star$, confirming the trends in Figs 1 and 3. The trend is weaker if we consider the progenitor bias, which affects mostly the lowest redshift bin (dashed lines in Figs 1 and 3). In the following we will try to reproduce these trends within the hierarchical framework. Galaxy mergers are the most accredited mechanisms that can account for both size and mass accretion, as we have also seen from the analysis of Section 4.1. Dissipationless major mergers from simulations in elliptical galaxies have predicted that the DM fraction within a certain physical radius decreases mildly after the merger (Boylan-Kolchin, Ma & Quataert 2005). But they have also shown that the DM fraction within the final R_e is greater than the DM fraction within the initial R_e, because the total mass within R_e, $M_{tot}(R_e)$, changes after the merger more than $M_\star(R_e)$. We have found the same result with real data (Fig. 3; Tortora et al. 2014c) and we have also found in Fig. 3 that this is also the case for a toy model that assumes the merging model from Hopkins et al. (2009) and the observed R_e–z relation. More recently, the problem has been investigated in detail with N-body simulations by Hilz et al. (2013). At different final stellar masses, they find that the equal-mass mergers produce

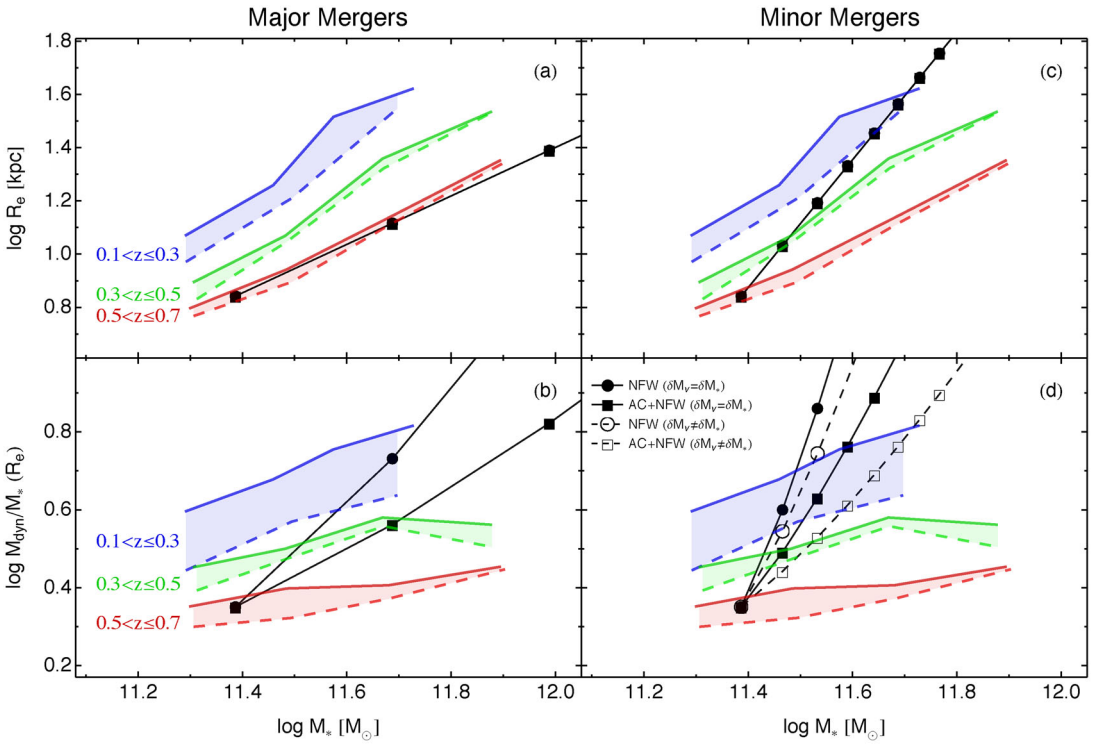

Figure 4. Evolution of R_e–$M_\star$ (panel a and c) and $M_{dyn}/M_\star$–$M_\star$ (panels b and d). Blue, green and red lines are for galaxies in three redshift bins $0.1 < z \leq 0.3$, $0.3 < z \leq 0.5$ and $0.5 < z \leq 0.7$. Solid lines are medians for the full sample, while dashed lines are for results corrected for progenitor bias. We take, as example, the average galaxy at $\log M_\star/M_\odot = 11.4$ and evolve it accordingly to the toy models discussed in the text. In the left-hand (right-hand) panels major (minor) merging predictions are shown. In the bottom panels (b and d), dots and filled squares are for NFW and AC+NFW profiles when $\delta M_\star = \delta M_{vir}$, and set the R_e, $M_\star$ and $M_{dyn}/M_\star$ after each single merging event. In panel (d), open circle and squares are for NFW and AC+NFW profiles when $\delta M_\star \neq \delta M_{vir}$.

a smaller size increase of multiple minor mergers. In particular, the variation of R_e with respect to the initial radius, R_e/R_0, in terms of the variation of $M_\star$ with respect to the initial stellar mass, $M_\star/M_0$, is found to be $R_e/R_0 \propto (M_\star/M_0)^{0.91}$ for the equal-mass merger and $\propto (M_\star/M_0)^{2.4}$ for the minor mergers (consistently with what was observed by van Dokkum et al. 2010).

Taking these results into account, we have constructed some toy models assuming that $M_{DM} \propto M_{vir} r^\eta$ around R_e, with $\eta \sim 2$ for a standard NFW and $\eta \sim 1.2$ for a contracted NFW, hereafter AC+NFW (according with Boylan-Kolchin et al. 2005). Following Hilz et al. (2013), we have also taken the average evolution of R_e in terms of $M_\star$ evolution for the equal-mass merging (i.e. $R_e/R_0 \propto (M_\star/M_0)^{0.91}$) and minor merging (i.e. $R_e/R_0 \propto (M_\star/M_0)^{2.4}$). Following Tortora et al. (2014c), we start assuming that the variation of the virial mass follows the one of the stellar mass, i.e. $\delta M_{vir} \approx \delta M_\star$. This intrinsically reflects the hypothesis that the systems participating to merging (i.e. the progenitors) all have the same $M_{vir}/M_\star$, which is reasonable for most of the stellar mass range covered by our sample. However, it is possible – mainly for the minor merging case – that the virial mass change at a different rate of the stellar mass, since the main galaxy is merging with another galaxy with a different $M_{vir}/M_\star$ (see e.g. table 2 in Boylan-Kolchin et al. 2005, where the final virial mass after the mergers is changed less than total stellar mass). These simplified models provide a quantitative assessment of the impact of the merging scenario on the observed DM fraction.

We have considered the evolution tracks related to the two different merging types (major and minor) for a galaxy with $\log M_\star/M_\odot = 11.4$. Dots and squares are for NFW and AC+NFW profiles, respectively. In Fig. 4 (the left-hand panels a and b), the major merging tracks are shown as black lines with dots/squares indicating the events corresponding to masses $\delta M_\star\, M_{\star,0}$, with the mass increments $\delta M_\star = 1, 2, 4, \ldots$, assuming that $\delta M_{vir} = \delta M_\star$. The first dot/square at $\log M_\star/M_\odot = 11.4$ corresponds to the initial progenitor galaxy. The second dot/square is the result of one major merger, which doubles the initial mass of the progenitor, while the third dot/square corresponds to a second major merger with mass four times the mass of the initial progenitor and two times the mass of the remnant of the first merging event. The minor merging tracks are shown in the right-hand panels (c and d) by black lines. Dots/squares indicate remnant with masses $M_{\star,0} + \delta M_\star\, M_{\star,0}$, where $\delta M_\star = 0, 0.2, 0.4, 0.6, \ldots$, and we use two different increment laws for M_{vir}. In panel (b) we use $\delta M_{vir} = \delta M_\star$. In panel (d) filled symbols are for $\delta M_{vir} = \delta M_\star$, while open symbols correspond to $\delta M_{vir} = 0.05 \delta M_\star$. In this case we suppose that the initial progenitor galaxy with mass $M_{\star,0}$ is experiencing a collection of minor mergers with galaxies having masses of 20 per cent of $M_{\star,0}$.

In order to determine which type of merging is describing the mass assembly of these massive galaxies we compare the model predictions with the data in Fig. 4. We plot the data without (with) progenitor bias as solid (dashed) lines. Blue, green and red lines are for galaxies in three redshift bins $0.1 < z \leq 0.3$, $0.3 < z \leq 0.5$ and $0.5 < z \leq 0.7$. We aim at whether mass, size and total-to-stellar mass evolution in KiDS galaxies can be explained, consistently, through major or minor mergers. We see that major mergers can be excluded, since the predicted evolution in size of a galaxy in the highest redshift bin (with $z \sim 0.6$) and with stellar mass $10^{11.4}\,M_\odot$ is parallel to the size–mass relation in this same redshift bin (see

left-hand panels in Fig. 4). On the contrary, the same galaxy can evolve to $z \sim 0.2$ experiencing few (five or six) minor mergers, which accrete ∼100 per cent of the initial stellar mass $M_{\star,0}$.

The example galaxy is not evolving on the top of the $z \sim 0.2$ R_e–$M_\star$ and $M_{dyn}/M_\star$–$M_\star$ relations if we consider that DM and star accrete at the same rate, for both NFW and AC+NFW (dots and filled squares in Fig. 4). The $M_{dyn}/M_\star$–$M_\star$ evolution is too steep, thus after ∼2 minor mergers the example galaxy would end up on the $z \sim 0.2$ observed $M_{dyn}/M_\star$–$M_\star$, this number is not consistent with what found analysing the R_e–$M_\star$ evolution, which would require 4–6 mergers to transform the $z \sim 0.6$ galaxy in a typical galaxy observed at $z \sim 0.2$. The number of minor mergers needed to transform the $z \sim 0.6$ galaxy in a bigger and more DM-dominated galaxy is found if the DM mass is accreting with a lower rate and only for the AC+NFW mass profile. This is possible if the main progenitor is merging with lower mass galaxies with smaller $M_{dyn}/M_\star$. This result suggests that our massive galaxy at $z \sim 0.6$ has to merge with a population of less massive galaxies with lower total-to-stellar mass ratios. Abundance matching studies predict the existence of these systems, since at stellar masses smaller than $10^{11.4}\,M_\odot$ galaxies are found to have, on average, smaller $M_{dyn}/M_\star$ (see e.g. Moster et al. 2010).

4.3 Systematics

There are different sources of systematics that may impact our results. We will list some of these systematics in the following.

(i) *KiDS versus SPIDER.* We have cross-matched the full matched DR7 sample (5223 galaxies) with the SDSS-based SPIDER data sample (39 993 galaxies), finding 248 galaxies with reliable structural parameters and masses in common. This sample spans the range of masses $\log M_\star/M_\odot \sim (10.2–11.4)$, which is different from the range used in this paper (i.e. $\log M_\star/M_\odot > 11.2$). We compare both structural parameters, stellar masses and velocity dispersions. Some differences are expected since the two samples rely on different image quality. Thus, while the median axis ratio is identical, and equal to $q_r = 0.7$, some small differences are found between KiDS and SPIDER in the effective radius (3.2 versus 2.9 arcsec) and Sérsic index (5.6 versus 5.3). The reason of this difference can probably be examined in the deepest KiDS images, which, including more light from the external regions, tend to produce larger sizes. However, these differences are within the typical measured uncertainties (see Roy et al., in preparation, for further details). Moreover, also stellar masses are consistent, with a median value of $\log M_\star M_\odot \sim 10.7$ dex. But, we caution the reader that KiDS and SDSS stellar masses are calculated using different photometric apertures (3 arcsec versus 3 times the *i*-band Kron radius), different wavelength coverage (optical versus optical+NIR) and different stellar population prescription (single-bursts versus exponential star formation). The aperture velocity dispersion is also consistent.

(ii) *Stellar mass modelling.* There are many systematics related to the stellar mass modelling. First of all, the $M_\star$ ($M_{dyn}/M_\star$) can become lower (higher) if we relax the constraints on age (e.g. by allowing ages lower than 3 Gyr) and metallicity (hence resuming the full Bruzual & Charlot 2003 synthetic library). The trends in terms of redshift are shallower, since the masses at larger redshifts are underestimated, as discussed in Maraston et al. (2013). Then, we have seen that median masses from LE PHARE are smaller or ∼0.05 dex if compared with the best-fitting values adopted in our analysis; however, the trends with redshift for $M_{dyn}/M_\star$ are quite similar. Then, stellar masses are negligibly affected if MAG_AUTO are adopted, instead of aperture magnitudes. The impact of stellar population templates is finally investigated for the BOSS data sample, comparing our inferences with BOSS values from Maraston et al. (2013). These BOSS masses are obtained fitting Maraston & Strömbäck (2011) passive templates (with ages older than 3 Gyr) to the u, g, r, i, z BOSS magnitudes. We have renormalized Maraston et al. (2013) stellar masses to a Chabrier IMF, by subtracting 0.05 dex, and converted to our cosmology by subtracting 0.035 dex, too. On average, our stellar masses are ∼0.08 dex larger, this discrepancy is related to differences in data sample and template prescription adopted. However, the difference is also stronger at $z \lesssim 0.5$, i.e. ∼0.12 dex, and is inverted at $0.6 \lesssim z \lesssim 0.7$, where our masses get smaller than BOSS estimates of ∼0.06 dex. The trends of $M_{dyn}/M_\star$ stay qualitatively the same. Thus, the results of this paper do not change if different stellar mass estimates are adopted, and conclusions are unaffected.

(iii) *Stellar mass uncertainties.* The median uncertainty of the Chabrier IMF stellar masses determined in Section 2.3 in our massive galaxy sample is ∼0.13 dex. We studied the impact of these uncertainties on our mass selection and all the trends discussed in this paper. We have randomly perturbed each mass, assuming a Gaussian with as mean the best-fitting mass and standard deviation the error of the best-fitting mass. Thus, we have selected the most massive galaxies with $\log M_\star/M_\odot > 11.2$, using the new perturbed masses. The impact on the $M_{dyn}/M_\star$–z trend is negligible.

(iv) *Stellar* M/L *gradients.* We already shown how the gradients impact the results by comparing the *g*- and *K*-band results for the SPIDER sample in Section 3. However, in general, at masses $\log M_\star/M_\odot > 11.2$ the colour and stellar M/L gradients are weak, thus the correction would be small (Tortora et al. 2011). Later analysis would also take into account possible gradients in the IMF (Martín-Navarro et al. 2015).

(v) *Mass profile slope.* In addition to uncertainties in stellar mass estimates, the choice of the mass profile can be inappropriate for lower σ_e (or $M_\star$) galaxies and cause an excess of negative $M_{dyn}/M_\star$ values, mainly at high-z (e.g. Sonnenfeld et al. 2013). In particular, $M_{dyn}/M_\star$ and the slope of total mass density are tightly correlated, with shallower density profiles corresponding to larger $M_{dyn}/M_\star$ (Humphrey & Buote 2010; Remus et al. 2013; Dutton & Treu 2014; Tortora et al. 2014b). To quantify the impact of a free-varying total mass density slope, α, we have adopted a power-law mass density $\rho \propto r^\alpha$, with slope steeper and shallower than isothermal. In Tortora et al. (2014c) we have shown that using two extreme values for the density slope, i.e. $\alpha = -2.5$ and -1.5, which bracket most of the results in the literature, then we find that the average $M_{dyn}/M_\star$ get smaller (larger) of ∼0.1 (∼0.05) dex for $\alpha = -2.5$ ($=-1.5$). However, in the realistic case with a varying slope with mass, smaller changes would be expected (Dutton & Treu 2014; Tortora et al. 2014b). If α is constant with time, then, at fixed mass, these corrections would shift all the results of the same factor, leaving naturally unaffected the observed trend with redshift. On the other hand, if we assume that the slope is varying with redshift, then the only way to totally remove any $M_{dyn}/M_\star$ evolution is that low- and high-redshift galaxies have systematically steeper (i.e. $\alpha < -2.5$) and shallower (i.e. $\alpha > -1.5$) mass density profiles than isothermal, and consequently smaller and larger $M_{dyn}/M_\star$. However, this is not expected since the most massive galaxies are found to have only more shallow profiles than isothermal at lower redshifts (e.g. Tortora et al. 2014b; Poci et al. 2017) and at high redshifts, where gas and in situ star formation dominate the galaxy evolution, the ETGs from cosmological simulations have a total density slope

very steep ($\alpha \sim -3$), with merging events driving the galaxy to a nearly isothermal profile (Remus et al. 2013, 2017). Xu et al. (2017) from the Illustris simulation find that α is constant with redshift, which would leave the trend unaffected. While, using strong lenses, Bolton et al. (2012) and Sonnenfeld et al. (2013) have shown that the total mass density slope is steeper at lower redshift. In particular, Sonnenfeld et al. (2013) find an average mass density slope of $\alpha \sim -2$ at $z \sim 0.65$ and $\alpha \sim -2.15$ at $z \sim 0.1$. Thus, at $z \sim 0.1$, $M_{\rm dyn}/M_\star$ would get smaller of $\sim$0.03 dex, leaving our trends almost unaffected. However, a varying slope with redshift has to be further investigated.

(vi) *Rotation velocity.* We have also neglected rotation correction, not accounted by the aperture velocity dispersion. If rotation velocities would be included in the analysis, $M_{\rm dyn}$ would get higher. But the impact would be negligible if compared with typical uncertainties. In the massive and high velocity dispersion galaxies analysed in this paper, this change would amount to $\sim$1 per cent (see Tortora et al. 2009).

(vii) *Orbital anisotropy.* The DM content of ETGs is estimated under the assumption that their stellar orbits are isotropic, which is incorrect at some level. Detailed dynamical modelling analysis has focused on the ETG central regions, finding anisotropies to be fairly mild in general, typically in the range $-0.2 \leq \beta \leq +0.3$ (Gerhard et al. 2001; Cappellari et al. 2007), where $\beta \equiv 1 - \sigma_\theta^2/\sigma_r^2$ quantifies the relative internal dispersions in the tangential and radial directions. Mild central anisotropy is also predicted from simulations of merger remnants (Dekel et al. 2005). The typical radial anisotropies found in local galaxies ($\beta \sim 0.2$), would decrease inferred dynamical masses by $\lesssim$5 per cent (i.e. $\lesssim$0.02 dex), lowering the $M_{\rm dyn}/M_\star$. Recently, using a sample of massive ($M_\star \gtrsim 10^{11}{\rm M}_\odot$) galaxies in the Illustris simulation, Xu et al. (2017) have predicted a gentle evolution in the average central anisotropy of their sample, from $\beta \sim -0.1$ at $z \sim 0.65$ to $\beta \sim 0.1$ at $z \sim 0.1$. This means that at $z \sim 0.1$ ($z \sim 0.65$) $M_{\rm dyn}/M_\star$ would be smaller (larger) of $\lesssim$3 per cent ($\lesssim$3 per cent), flattening our $M_{\rm dyn}/M_\star$–z trend. However, the impact on our results is negligible.

(viii) *Ellipticity.* We have checked the effect of the ellipticity in the mass inferences and restricted the analysis to KiDS objects with axis ratio $q > 0.6$ (86 per cent of the sample), in order to limit to the roundest galaxies. The overall results are practically unchanged.

(ix) *Sérsic index selection.* We have also checked if the results are affected if we select those objects with large Sérsic indices (i.e. r-band $n > 2.5$), typical of most of the ETGs (Tortora et al. 2010a). This high-n sample consists of $\sim$94 per cent of the original sample of massive galaxies. The impact on the results is negligible, too.

(x) *Rest-frame structural parameters.* We have derived rest-frame structural parameters by fitting a straight line $\log X = a + b\log\lambda$ to the data points (λ_l, X_l) at the three KiDS wavebands g, r and i. To study the impact of this choice, we have also replaced the straight line with the polynomial function $\log X = a + b\log\lambda + c(\log\lambda)^2$. The impact on our results is negligible, since the difference between the derived Sérsic index, effective radius and $M_{\rm dyn}/M_\star$ using the two fitting functions is smaller than 3 per cent.

(xi) We do not include in the mass model the black hole, but we have calculated that its effect is, on average, negligible, with an impact on $M_{\rm dyn}$ of $\sim$2 per cent (Tortora et al. 2009).

5 CONCLUSIONS

We have analysed the central DM content in a sample of massive ($\log M_\star/{\rm M}_\odot > 11.2$) ETGs at redshift $\lesssim$0.7 from KiDS, a VST public survey (de Jong et al. 2015, 2017). Thanks to the excellent seeing condition at Paranal, the small pixel scale (0.2 arcsec pixel^{-1}) and the depth of the survey, KiDS provides us with high-quality images. We extract a sample of galaxies with S/N > 50, with masses and structural parameters from 156 deg^2 of the KiDS survey, and spectroscopic coverage from SDSS-DR7 and SDSS/BOSS data samples. With spectroscopic redshifts, structural parameters, stellar masses and velocity dispersion for a sample of 3778 massive ($\log M_\star/{\rm M}_\odot > 11.2$) galaxies, we can rely on the ideal data sample to perform the isotropic Jeans dynamical analysis and study the central DM content, parametrized through the total-to-stellar mass ratio, $M_{\rm dyn}/M_\star$ (calculated at $r = 1{\rm R_e}$; Tortora et al. 2009, 2012, 2014c).

We have shown that the local relationships between $M_{\rm dyn}/M_\star$ and effective radius $R_{\rm e}$, Sérsic index n, velocity dispersion within effective radius $\sigma_{\rm e}$, stellar mass $M_\star$, central average stellar density $\langle\rho_\star\rangle$ and dynamical mass $M_{\rm dyn}$ conserve their trends at larger redshifts. These correlations are shown in Fig. 1. We find that larger galaxies with steeper light profiles (large ns) are more DM dominated. The effective radius is the main driver of all the correlations. A similar steep trend is found in terms of $M_{\rm dyn}$ and $\sigma_\star$. On the contrary, $M_{\rm dyn}/M_\star$ vary weakly in terms of $M_\star$, while we find a steep anticorrelation with central average stellar density. These results confirm most of the previous literature at $z \sim 0$ (Padmanabhan et al. 2004; Cappellari et al. 2006; Hyde & Bernardi 2009a; Tortora et al. 2009, 2012; Napolitano et al. 2010), or at intermediate redshift (Auger et al. 2010; Tortora et al. 2010b, 2014c; Barnabè et al. 2011).

However, one of the most important result of this paper is that the central DM is evolving from high- to low-z, with less DM at higher redshift. At fixed mass, we find that the galaxies in the highest redshift bin have $M_{\rm dyn}/M_\star$ $\sim$0.2–0.4 dex smaller than local galaxies. Our findings are qualitatively consistent with results in Beifiori et al. (2014) and Tortora et al. (2014c). We have also investigated the evolution of $R_{\rm e}$, $\sigma_{\rm e}$ and $M_{\rm dyn}/M_\star$ within various galaxy formation scenarios. We exclude the PS from active galactic nuclei (AGN) feedback in Fan et al. (2008), since this kind of process produces very high $\sigma_{\rm e}$ and $M_{\rm dyn}/M_\star$ at higher z, not observed. The predictions from galaxy merging scenario from Hopkins et al. (2009) are consistent with the observed size and mass growth with z (Fig. 3).

We find that the fraction of galaxies with negative DM are increasing with redshift, but for the massive galaxies under analysis a Chabrier or Salpeter IMF cannot be excluded. This result is not in contrast with the recent findings in Shetty & Cappellari (2014), who find a Salpeter IMF in $z \sim 0.75$ massive galaxies. We have also shown (fixing the DM fraction) how the trends of $M_{\rm dyn}/M_\star$ could be interpreted within the context of a non-universal IMF, pointing to a varying IMF in terms of the galaxy properties (Tortora et al. 2013, 2014a,b). If we assume a constant DM fraction with redshift, then the observed change of $M_{\rm dyn}/M_\star$ is driven by an evolution of the IMF (panels g and h of Fig. 3). IMF is found to vary from a Chabrier or Salpeter IMF at $z \sim 0.65$ to a super-Salpeter or very steep IMF at low redshift. However, it is difficult to explain this evolution within the galaxy formation scenario, and in particular through galaxy mergers, since the combination of a 'higher' (e.g. bottom-heavier) and a 'lower' mass (e.g. bottom-lighter) IMF would produce a dilution in the IMF shape, i.e. this process will not produce a more bottom-heavy IMF, but an intermediate IMF slope. The mergers would decrease $\delta_{\rm IMF}$ or leave it almost constant with redshift, as predicted by the galaxy merging toy models in Sonnenfeld et al. (2017), contrasting the evolution seen in Fig. 3, and suggesting that $f_{\rm DM}$ need to evolve with cosmic time. However, a detailed analysis of the joint IMF and DM fraction evolution across the time is beyond the scope of this paper. We will address this

issue in future, assuming more complex mass modelling (Tortora et al. 2013, 2014a,b, 2016).

Finally, to have a more conclusive answer about the physical processes leading the evolution of these massive galaxies, we have studied how R_e–$M_\star$ and $M_{dyn}/M_\star$–$M_\star$ correlations change with redshift. And we have used toy models to investigate how this evolution can be explained by the mass accretion from minor and major mergings (Boylan-Kolchin et al. 2005; Hilz et al. 2013; Tortora et al. 2014c). We find that our results point to minor mergers as main driver of the mass accretion, since major mergers would produce a too strong mass accretion, which is not observed (Fig. 4, the size evolution is parallel to the R_e–$M_\star$ relation for galaxies at the same redshift). To consistently reproduce the evolution in both the size and $M_{dyn}/M_\star$, then, we have demonstrated that the accretion of total DM mass would be weaker than the stellar mass one. This can be achieved if the main galaxy is merging with lower mass galaxies with a smaller $M_{dyn}/M_\star$. This result is consistent with independent studies that find that $M_{dyn}/M_\star$ is getting smaller at lower masses, down to the threshold mass of $\sim 10^{10.5}$ $M_\odot$, translating to a star formation efficiency that is increasing from large and massive galaxies to intermediate-mass galaxies (Benson et al. 2000; Marinoni & Hudson 2002; Napolitano et al. 2005; Mandelbaum et al. 2006; van den Bosch et al. 2007; Conroy & Wechsler 2009; Moster et al. 2010).

In a future work we will perform a more systematic study of the IMF, to investigate if it can be considered universal with cosmic time, or if it is changing as a function of the redshift. Then, we plan to have 10 times more galaxies at the end of the KiDS survey, when all the 1500 deg^2 will have been observed.

ACKNOWLEDGEMENTS

We thank the anonymous referee for comments. CT and LVEK are supported through an NWO-VICI grant (project number 639.043.308). KHK acknowledges support by the Alexander von Humboldt Foundation. GAVK acknowledges financial support from the Netherlands Research School for Astronomy (NOVA) and Target. Target is supported by Samenwerkingsverband Noord Nederland, European fund for regional development, Dutch Ministry of economic affairs, Pieken in de Delta, Provinces of Groningen and Drenthe. This study is based on data products from observations made with ESO Telescopes at the La Silla Paranal Observatory under programme IDs 177.A-3016, 177.A-3017 and 177.A-3018, and on data products produced by Target/OmegaCEN, INAF-OACN, INAF-OAPD and the KiDS production team, on behalf of the KiDS consortium. OmegaCEN and the KiDS production team acknowledge support by NOVA and NWO-M grants. Members of INAF-OAPD and INAF-OACN also acknowledge the support from the Department of Physics and Astronomy of the University of Padova, and of the Department of Physics of Univ. Federico II (Naples).

REFERENCES

Abazajian K. et al., 2003, AJ, 126, 2081
Abazajian K. N. et al., 2009, ApJS, 182, 543
Adelman-McCarthy J. K. et al., 2008, ApJS, 175, 297
Ahn C. P. et al., 2014, ApJS, 211, 17
Alabi A. B. et al., 2016, MNRAS, 460, 3838
Arnouts S., Cristiani S., Moscardini L., Matarrese S., Lucchin F., Fontana A., Giallongo E., 1999, MNRAS, 310, 540
Auger M. W., Treu T., Bolton A. S., Gavazzi R., Koopmans L. V. E., Marshall P. J., Bundy K., Moustakas L. A., 2009, ApJ, 705, 1099
Auger M. W., Treu T., Bolton A. S., Gavazzi R., Koopmans L. V. E., Marshall P. J., Moustakas L. A., Burles S., 2010, ApJ, 724, 511
Barnabè M., Czoske O., Koopmans L. V. E., Treu T., Bolton A. S., 2011, MNRAS, 415, 2215
Barnabè M., Spiniello C., Koopmans L. V. E., Trager S. C., Czoske O., Treu T., 2013, MNRAS, 436, 253
Bastian N., Covey K. R., Meyer M. R., 2010, ARA&A, 48, 339
Beifiori A. et al., 2014, ApJ, 789, 92
Benson A. J., Cole S., Frenk C. S., Baugh C. M., Lacey C. G., 2000, MNRAS, 311, 793
Blumenthal G. R., Faber S. M., Primack J. R., Rees M. J., 1984, Nature, 311, 517
Bolton A. S., Burles S., Koopmans L. V. E., Treu T., Moustakas L. A., 2006, ApJ, 638, 703
Bolton A. S., Burles S., Koopmans L. V. E., Treu T., Gavazzi R., Moustakas L. A., Wayth R., Schlegel D. J., 2008, ApJ, 682, 964
Bolton A. S. et al., 2012, ApJ, 757, 82
Boylan-Kolchin M., Ma C.-P., Quataert E., 2005, MNRAS, 362, 184
Bruzual G., Charlot S., 2003, MNRAS, 344, 1000
Buitrago F., Trujillo I., Conselice C. J., Bouwens R. J., Dickinson M., Yan H., 2008, ApJ, 687, L61
Bullock J. S., Kolatt T. S., Sigad Y., Somerville R. S., Kravtsov A. V., Klypin A. A., Primack J. R., Dekel A., 2001, MNRAS, 321, 559
Cappellari M., Emsellem E., 2004, PASP, 116, 138
Cappellari M. et al., 2006, MNRAS, 366, 1126
Cappellari M. et al., 2007, MNRAS, 379, 418
Cappellari M. et al., 2012, Nature, 484, 485
Cappellari M. et al., 2013, MNRAS, 432, 1862
Cardone V. F., Tortora C., 2010, MNRAS, 409, 1570
Cardone V. F., Tortora C., Molinaro R., Salzano V., 2009, A&A, 504, 769
Cardone V. F., Del Popolo A., Tortora C., Napolitano N. R., 2011, MNRAS, 416, 1822
Cenarro A. J., Trujillo I., 2009, ApJ, 696, L43
Chabrier G., 2001, ApJ, 554, 1274
Chae K.-H., Bernardi M., Kravtsov A. V., 2014, MNRAS, 437, 3670
Conroy C., van Dokkum P. G., 2012, ApJ, 760, 71
Conroy C., Wechsler R. H., 2009, ApJ, 696, 620
Conselice C. J., 2014, ARA&A, 52, 291
Corsini E. M., Wegner G. A., Thomas J., Saglia R. P., Bender R., 2017, MNRAS, 466, 974
Daddi E. et al., 2005, ApJ, 626, 680
de Jong J. T. A. et al., 2015, A&A, 582, A62
de Jong J. T. A. et al., 2017, A&A, 604, A134
Dekel A., Stoehr F., Mamon G. A., Cox T. J., Novak G. S., Primack J. R., 2005, Nature, 437, 707
de Vaucouleurs G., 1948, Ann. d'Astrophys., 11, 247
Dutton A. A., Treu T., 2014, MNRAS, 438, 3594
Dutton A. A., Macciò A. V., Mendel J. T., Simard L., 2013, MNRAS, 432, 2496
Eisenstein D. J. et al., 2011, AJ, 142, 72
Fan L., Lapi A., De Zotti G., Danese L., 2008, ApJ, 689, L101
Faure C. et al., 2011, A&A, 529, A72
Ferreras I., La Barbera F., de la Rosa I. G., Vazdekis A., de Carvalho R. R., Falcón-Barroso J., Ricciardelli E., 2013, MNRAS, 429, L15
Gallazzi A., Charlot S., Brinchmann J., White S. D. M., Tremonti C. A., 2005, MNRAS, 362, 41
Gavazzi R., Treu T., Rhodes J. D., Koopmans L. V. E., Bolton A. S., Burles S., Massey R. J., Moustakas L. A., 2007, ApJ, 667, 176
Gerhard O., Kronawitter A., Saglia R. P., Bender R., 2001, AJ, 121, 1936
Gnedin O. Y., Kravtsov A. V., Klypin A. A., Nagai D., 2004, ApJ, 616, 16
Gnedin O. Y., Weinberg D. H., Pizagno J., Prada F., Rix H.-W., 2007, ApJ, 671, 1115
Goudfrooij P., Kruijssen J. M. D., 2013, ApJ, 762, 107
Goudfrooij P., Kruijssen J. M. D., 2014, ApJ, 780, 43
Graves G. J., Faber S. M., Schiavon R. P., 2009, ApJ, 698, 1590
Grillo C., 2010, ApJ, 722, 779
Grillo C., Gobat R., 2010, MNRAS, 402, L67

Grillo C., Gobat R., Lombardi M., Rosati P., 2009, A&A, 501, 461
Hilz M., Naab T., Ostriker J. P., 2013, MNRAS, 429, 2924
Hopkins P. F., Hernquist L., Cox T. J., Keres D., Wuyts S., 2009, ApJ, 691, 1424
Humphrey P. J., Buote D. A., 2010, MNRAS, 403, 2143
Hyde J. B., Bernardi M., 2009a, MNRAS, 394, 1978
Hyde J. B., Bernardi M., 2009b, MNRAS, 396, 1171
Ilbert O. et al., 2006, A&A, 457, 841
Jorgensen I., Franx M., Kjaergaard P., 1995, MNRAS, 273, 1097
Khochfar S., Silk J., 2006, ApJ, 648, L21
Kochanek C. S., 1991, ApJ, 373, 354
Komatsu E. et al., 2011, ApJS, 192, 18
Koopmans L. V. E., Treu T., Bolton A. S., Burles S., Moustakas L. A., 2006, ApJ, 649, 599
La Barbera F., de Carvalho R. R., 2009, ApJ, 699, L76
La Barbera F., de Carvalho R. R., Kohl-Moreira J. L., Gal R. R., Soares-Santos M., Capaccioli M., Santos R., Sant'anna N., 2008, PASP, 120, 681
La Barbera F., de Carvalho R. R., de La Rosa I. G., Lopes P. A. A., Kohl-Moreira J. L., Capelato H. V., 2010, MNRAS, 408, 1313
La Barbera F., Ferreras I., Vazdekis A., de la Rosa I. G., de Carvalho R. R., Trevisan M., Falcón-Barroso J., Ricciardelli E., 2013, MNRAS, 433, 3017
Li H. et al., 2017, ApJ, 838, 77
Lyubenova M. et al., 2016, MNRAS, 463, 3220
Macciò A. V., Dutton A. A., van den Bosch F. C., 2008, MNRAS, 391, 1940
McDermid R. M. et al., 2014, ApJ, 792, L37
Mandelbaum R., Seljak U., Kauffmann G., Hirata C. M., Brinkmann J., 2006, MNRAS, 368, 715
Maraston C., Strömbäck G., 2011, MNRAS, 418, 2785
Maraston C., Strömbäck G., Thomas D., Wake D. A., Nichol R. C., 2009, MNRAS, 394, L107
Maraston C. et al., 2013, MNRAS, 435, 2764
Marinoni C., Hudson M. J., 2002, ApJ, 569, 101
Martín-Navarro I., Barbera F. L., Vazdekis A., Falcón-Barroso J., Ferreras I., 2015, MNRAS, 447, 1033
Mehlert D., Saglia R. P., Bender R., Wegner G., 2000, A&AS, 141, 449
Moster B. P., Somerville R. S., Maulbetsch C., van den Bosch F. C., Macciò A. V., Naab T., Oser L., 2010, ApJ, 710, 903
Napolitano N. R. et al., 2005, MNRAS, 357, 691
Napolitano N. R., Romanowsky A. J., Tortora C., 2010, MNRAS, 405, 2351
Navarro J. F., Frenk C. S., White S. D. M., 1996, ApJ, 462, 563 (NFW)
Nigoche-Netro A. et al., 2016, MNRAS, 462, 951
Oguri M., Rusu C. E., Falco E. E., 2014, MNRAS, 439, 2494
Padmanabhan N. et al., 2004, New Astron., 9, 329
Poci A., Cappellari M., McDermid R. M., 2017, MNRAS, 467, 1397
Posti L., Nipoti C., Stiavelli M., Ciotti L., 2014, MNRAS, 440, 610
Remus R.-S., Burkert A., Dolag K., Johansson P. H., Naab T., Oser L., Thomas J., 2013, ApJ, 766, 71
Remus R.-S., Dolag K., Naab T., Burkert A., Hirschmann M., Hoffmann T. L., Johansson P. H., 2017, MNRAS, 464, 3742
Roche N., Bernardi M., Hyde J., 2010, MNRAS, 407, 1231
Ruff A. J., Gavazzi R., Marshall P. J., Treu T., Auger M. W., Brault F., 2011, ApJ, 727, 96
Rusin D., Kochanek C. S., Keeton C. R., 2003, ApJ, 595, 29
Ruszkowski M., Springel V., 2009, ApJ, 696, 1094
Saglia R. P., Maraston C., Greggio L., Bender R., Ziegler B., 2000, A&A, 360, 911
Saglia R. P. et al., 2010, A&A, 524, A6
Salpeter E. E., 1955, ApJ, 121, 161
Sarzi M. et al., 2006, MNRAS, 366, 1151
Schlafly E. F., Finkbeiner D. P., 2011, ApJ, 737, 103
Shankar F., Bernardi M., 2009, MNRAS, 396, L76
Shankar F., Marulli F., Bernardi M., Dai X., Hyde J. B., Sheth R. K., 2010, MNRAS, 403, 117
Shetty S., Cappellari M., 2014, ApJ, 786, L10
Shu Y. et al., 2015, ApJ, 803, 71
Smith R. J., Lucey J. R., Conroy C., 2015, MNRAS, 449, 3441
Sonnenfeld A., Treu T., Gavazzi R., Suyu S. H., Marshall P. J., Auger M. W., Nipoti C., 2013, ApJ, 777, 98
Sonnenfeld A., Treu T., Marshall P. J., Suyu S. H., Gavazzi R., Auger M. W., Nipoti C., 2015, ApJ, 800, 94
Sonnenfeld A., Nipoti C., Treu T., 2017, MNRAS, 465, 2397
Sparks W. B., Jorgensen I., 1993, AJ, 105, 1753
Spiniello C., Trager S. C., Koopmans L. V. E., Chen Y. P., 2012, ApJ, 753, L32
Spiniello C., Barnabè M., Koopmans L. V. E., Trager S. C., 2015, MNRAS, 452, L21
Swindle R., Gal R. R., La Barbera F., de Carvalho R. R., 2011, AJ, 142, 118
Thomas D., Maraston C., Bender R., Mendes de Oliveira C., 2005, ApJ, 621, 673
Thomas J., Saglia R. P., Bender R., Thomas D., Gebhardt K., Magorrian J., Corsini E. M., Wegner G., 2007, MNRAS, 382, 657
Thomas J., Saglia R. P., Bender R., Thomas D., Gebhardt K., Magorrian J., Corsini E. M., Wegner G., 2009, ApJ, 691, 770
Thomas J. et al., 2011, MNRAS, 415, 545
Thomas D. et al., 2013, MNRAS, 431, 1383
Tortora C., Napolitano N. R., Romanowsky A. J., Capaccioli M., Covone G., 2009, MNRAS, 396, 1132
Tortora C., Napolitano N. R., Cardone V. F., Capaccioli M., Jetzer P., Molinaro R., 2010a, MNRAS, 407, 144
Tortora C., Napolitano N. R., Romanowsky A. J., Jetzer P., 2010b, ApJ, 721, L1
Tortora C., Napolitano N. R., Romanowsky A. J., Jetzer P., Cardone V. F., Capaccioli M., 2011, MNRAS, 418, 1557
Tortora C., La Barbera F., Napolitano N. R., de Carvalho R. R., Romanowsky A. J., 2012, MNRAS, 425, 577
Tortora C., Romanowsky A. J., Napolitano N. R., 2013, ApJ, 765, 8
Tortora C., Romanowsky A. J., Cardone V. F., Napolitano N. R., Jetzer P., 2014a, MNRAS, 438, L46
Tortora C., La Barbera F., Napolitano N. R., Romanowsky A. J., Ferreras I., de Carvalho R. R., 2014b, MNRAS, 445, 115
Tortora C., Napolitano N. R., Saglia R. P., Romanowsky A. J., Covone G., Capaccioli M., 2014c, MNRAS, 445, 162
Tortora C., La Barbera F., Napolitano N. R., 2016, MNRAS, 455, 308
Tortora C., Koopmans L. V. E., Napolitano N. R., 2017, preprint (arXiv:1702.08865)
Treu T., Koopmans L. V. E., 2004, ApJ, 611, 739
Treu T., Auger M. W., Koopmans L. V. E., Gavazzi R., Marshall P. J., Bolton A. S., 2010, ApJ, 709, 1195
Trujillo I., Burkert A., Bell E. F., 2004, ApJ, 600, L39
Trujillo I. et al., 2006, ApJ, 650, 18
Trujillo I., Conselice C. J., Bundy K., Cooper M. C., Eisenhardt P., Ellis R. S., 2007, MNRAS, 382, 109
Trujillo I., Ferreras I., de La Rosa I. G., 2011, MNRAS, 415, 3903
Valentinuzzi T. et al., 2010a, ApJ, 712, 226
Valentinuzzi T. et al., 2010b, ApJ, 721, L19
van den Bosch F. C. et al., 2007, MNRAS, 376, 841
van der Wel A., Holden B. P., Zirm A. W., Franx M., Rettura A., Illingworth G. D., Ford H. C., 2008, ApJ, 688, 48
van Dokkum P. G., Conroy C., 2010, Nature, 468, 940
van Dokkum P. G., Franx M., 2001, ApJ, 553, 90
van Dokkum P. G. et al., 2010, ApJ, 709, 1018
Vulcani B. et al., 2014, MNRAS, 441, 1340
Wegner G. A., Corsini E. M., Thomas J., Saglia R. P., Bender R., Pu S. B., 2012, AJ, 144, 78
Weidner C., Ferreras I., Vazdekis A., La Barbera F., 2013, MNRAS, 435, 2274
Wu X., Gerhard O., Naab T., Oser L., Martinez-Valpuesta I., Hilz M., Churazov E., Lyskova N., 2014, MNRAS, 438, 2701
Xu D., Springel V., Sluse D., Schneider P., Sonnenfeld A., Nelson D., Vogelsberger M., Hernquist L., 2017, MNRAS, 469, 1824

This paper has been typeset from a TEX/LATEX file prepared by the author.